Origins of the giant magnetoplastic effect in $L2_1$-ordered intermetallics

Bailey E. Rhodes,[1,*] Justin A. Mayer,[1] W. Streit Cunningham,[1,2] Arda Genc,[1] Solène Comby-Dassonneville,[3] Thomas W. Cornelius,[3] Olivier Thomas,[3] Ram Seshadri,[1,4] Yolita M. Eggeler,[5] Irene J. Beyerlein,[1,6] and Daniel S. Gianola[1,†]

[1]*Materials Department, University of California, Santa Barbara, California 93106, USA*
[2]*Department of Materials Science and Engineering, University of Virginia, Charlottesville, Virginia 22904, USA*
[3]*Aix Marseille Univ, Univ Toulon, CNRS, IM2NP UMR 7334, Marseille, France*
[4]*Department of Chemistry and Biochemistry, University of California, Santa Barbara, California 93106, USA*
[5]*Laboratory for Electron Microscopy, Karlsruhe Institute of Technology, Karlsruhe D-76131, Germany*
[6]*Mechanical Engineering Department, University of California, Santa Barbara, California 93106, USA*

(Received 2 July 2025; revised 1 March 2026; accepted 11 March 2026; published 8 May 2026)

Microstructural engineering represents a promising avenue toward controlling the macroscopic response of high-performance magnetic materials, yet the physical origins linking microstructure to magnetic properties remain to be fully established. In this contribution, we establish magnetoplastic control over macroscopic magnetic properties by inducing high densities of extended lattice defects within the prototypical $L2_1$-ordered intermetallic $MnCu_2Al$, which serves as an ideal model system. We demonstrate a nearly 95% decrease in the initial net saturation magnetization following a high degree of plastic deformation, with effects that are reversible through annealing. Synchrotron X-ray diffraction and scanning electron nanodiffraction permit microscopic correlation of the changes in magnetic behavior with increasing defect content. Microstructural characterization at the single defect level, coupled with detailed first-principles modeling, suggests the presence of a local antiferromagnetic coupling within the extended defects that is at the origin of the dramatic magnetoplastic effect in these magnetic intermetallics. We ascribe these effects to the planar dissociation of dislocations hosting intervening antiphase boundaries, altering the atomic environment and, in turn, the magnetic coupling in the vicinity of dislocations.

DOI: 10.1103/k8bj-j1tp

I. INTRODUCTION

Magnetic materials and their integration in devices are central actors in the global effort towards electrification and a modernized, environmentally friendly energy economy, as exemplified in applications such as electrified transportation, efficient magnetic refrigeration, and low-power, high-performance, computing devices [1,2]. Achieving control over the magnetic structure in such materials requires a delicate interplay of materials design that promotes favorable magnetic spin interactions and avenues for tunability of spin textures through external stimuli, such as temperature, electric field, or pressure. In ferromagnetic materials, for example, additional control can be exerted through alloying or through partial site and/or chemical disorder. When the chemically disordered state is an antiferromagnetic or paramagnetic phase, this results in a partial decrease in the saturation magnetization of the ordered soft ferromagnetic phase, reliant on the extent of disorder [Fig. 1(a)]. Additional control can be engineered using microstructural elements that primarily affect the macroscopic coercivity of the resulting material, such as crystalline texture, grain boundaries, twin boundaries, precipitates, dislocation networks, and porosity. For instance, an increase in the stored dislocation density can reduce the rate of magnetization processes through domain wall motion (in the form of both domain nucleation and pinning), enabling the retention of magnetization after the reversal of the applied field [Fig. 1(a)] [3,4]. Independently harnessing these degrees of freedom to optimize the magnetic properties remains challenging, and is often constrained by the synthesis and processing requirements of the macroscopic material [5].

Indeed, a material class where defect structures introduced through thermal processing have been linked to distinct magnetic environments is the Mn-based $L2_1$-ordered intermetallics. $L2_1$-ordered intermetallics (also known as Heusler intermetallics) crystallize with the $Fm\bar{3}m$ space group, with the stoichiometry XY_2Z [8,9]. $L2_1$-ordered intermetallics with the general formula MnY_2Z typically exhibit ferromagnetism, wherein the Mn moments are coupled through Ruderman-Kittel-Kasuya-Yosida (RKKY)-type exchange, facilitated by the Z component [10–12]. Although the RKKY coupling model is a simplified model that relies on the assumption that the Y and Z constituents are nonmagnetic and do not participate in direct exchange, it provides a basis for the oscillatory relationship between ferromagnetic and antiferromagnetic coupling that is observed in Mn-based $L2_1$ intermetallics [13,14]. The RKKY coupling model matches experiments conducted using inelastic neutron

*Contact author: baileyrhodes@ucsb.edu
†Contact author: gianola@ucsb.edu

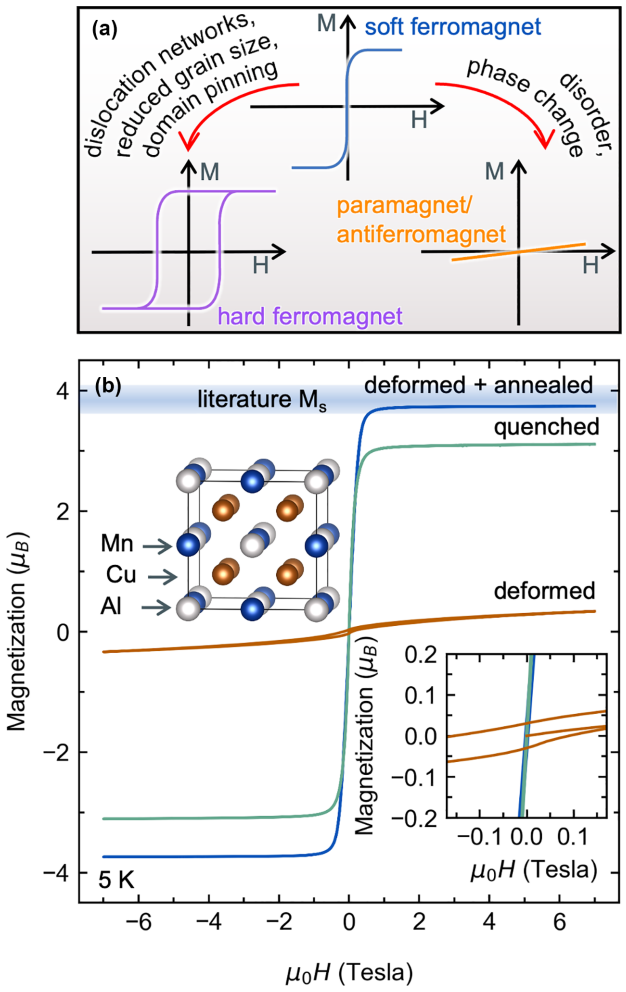

FIG. 1. (a) Schematic of processing routes that impact the magnetic properties of an initially soft ferromagnetic material. (b) M–H curves of $MnCu_2Al$ in the deformed + annealed, quenched, and deformed conditions. The highlighted band shows literature saturation magnetization (M_s) values for the pristine compound [6,7]. All data were collected at 5 K. The inset shows the difference in coercivity near zero field. A schematic of $MnCu_2Al$ in the $L2_1$ (Heusler) crystal structure is also inset.

scattering in $L2_1$-ordered $MnNi_2Sn$ [15], $MnPd_2Sn$ [15], and $MnCu_2Al$ [16].

The oscillatory relationship between the coupling constant (J) and the interatomic distances of the Mn atoms in Mn-based $L2_1$ intermetallics, combined with unit cells that are derived from orderings on a simpler lattice, implies that certain modes of crystalline slip via plastic deformation have the potential to place atoms on new lattice sites, thus creating new Mn–Mn interatomic coupling distances where antiferromagnetic coupling is favored. Specific examples would include the passage of partial dislocations that do not fully restore the original ordering, or the presence of dissociated dislocations comprising partial dislocations bounding planar fault structures. This rationale has been employed to describe the anomalous decrease in net saturation magnetization (M_s) observed by quenching the $L2_1$-ordered intermetallics from elevated temperatures [17–22]. The reduction in M_s was found to coincide with the formation of ⟨100⟩{010}-type antiphase boundaries. The density of antiphase boundaries and reduction in M_s were reversible with annealing treatments.

Lapworth and Jakubovics provided the first direct evidence of the antiferromagnetic character of the defect structures generated in $MnCu_2Al$ by quenching using Lorentz transmission electron microscopy (TEM), as the ferromagnetic domain structures were observed to be pinned by the defects [17]. The antiferromagnetic coupling of quenched-in ⟨100⟩{010}-type defect structures generated in $MnNi_2Ga$ by quenching has also locally been established using Lorentz TEM by Venkateswaren *et al.* [23], where the local antiferromagnetic character manifested as an apparent local reversal of the ferromagnetic induction. Similar results were observed using magnetic force microscopy by Straka *et al.* [24]. This phenomenon has been studied in $MnCu_2Al$ [17,18] and in $MnNi_2Ga$ [23–25], but the magnitude of the reduction in M_s associated with the ⟨100⟩{010} defects from quenching was limited to a maximum of 30% of the initial value.

Much greater reductions in M_s can be achieved by using plastic deformation as a method of generating planar faults, owing to the higher density of defect structures achievable through deformation. However, whether the defect generation is thermal in nature or through plastic deformation will likely influence the defect type and its detailed character. The magnetic response to plastic deformation has been studied in $MnPd_2Sn$ [19–21], $MnNi_2Sn$ [19], and $MnAu_2Al$ [22] and has resulted in a reduction in M_s up to 85% of the pristine value. However, the complex microstructures that are endemic to such highly deformed materials have so far hindered efforts to (1) locally characterize the antiferromagnetic character of the defect structures and (2) correlate the net changes in M_s to the density of the defect population, because of the presence of complex contrast present in TEM investigations of the deformed microstructures. Nevertheless, through their studies of $MnCu_2Al$, Lapworth and Jakubovics found that the ⟨111⟩ dislocation structures generated by deformation to small plastic strains had a much stronger domain pinning effect than those generated by quenching [17], but were unable to resolve further details of the partial dislocations delineating fault structures or correlate the defect density to a macroscopic change in magnetic properties. Dislocations in this system that are generated by plastic deformation are thought to dissociate into partial dislocations, with a reaction that takes the approximate form:

$$[111] = \tfrac{1}{4}[111] + \tfrac{1}{4}[111] + \tfrac{1}{4}[111] + \tfrac{1}{4}[111], \qquad (1)$$

both on the {110} or {112} planes [17,26,27]. The large extinction distances of these ⟨111⟩{110}-type defect structures [23,24], coupled with compact fault widths that are characteristic of BCC-derived intermetallics [17,28], have led to challenges in the characterization of the defect structures generated by plastic deformation. Using weak beam microscopy, Green *et al.* were able to identify pairs of dislocations in $MnCu_2Al$ with ⟨111⟩ Burgers vectors, implying the coupling of partial dislocations to restore chemical ordering, but the expected fourfold splitting of individual dislocations could not be resolved [26]. Rhodes *et al.* recently performed phase-field dislocation dynamics simulations to corroborate the splitting predicted in Eq. (1) [28]. It was predicted that the dissociation reactions between the edge and screw dislocations were

different and both possess antiphase boundaries within the extended defect. The impact of these structures on magnetic properties have not yet been systematically studied.

Here, we aim to control the macroscopic magnetic properties in $MnCu_2Al$ by introducing high densities of defects that locally produce antiferromagnetic interactions that are not otherwise present in the macroscopic material. We use an array of thermal and mechanical processing approaches and a suite of characterization methods to disentangle the potential effects of chemical disorder from those that arise from thermally and mechanically induced defect structures. We demonstrate a reduction of the initial M_s to a value reduced by 95.4% and with nonsaturating behavior following heavy plastic deformation, thereby demonstrating a giant magnetoplastic effect. We design and employ microscale mechanical testing specimens that facilitate single defect characterization, which suggests local antiferromagnetic order present at the defects. Our work directly links the local magnetic properties of the defect structures generated by plastic deformation to the pronounced changes in macroscopic magnetic response, thereby elucidating the origin of magnetoplastic control in Mn-based $L2_1$-ordered materials and paving the way for materials design that profits from this effect.

II. MATERIALS AND METHODS

$L2_1$-ordered intermetallic $MnCu_2Al$ was processed, as described previously [17,18,28–31], through arc melting high-purity starting materials, followed by an annealing treatment at 850°C within a sealed silica ampule and quenching the sealed silica ampule containing the sample into water (Fig. 2). Part of the ingot was ground into a fine powder using a mortar and pestle, sieved through a 140 mesh (106 μm particle size) and tempered at 320°C for 1 hour. Powders labeled "deformed + annealed" were not treated any further beyond this state. "Deformed" powder was created from the deformed + annealed state by grinding in a mortar and pestle for approximately 10 minutes at room temperature. Deformation and all subsequent processing of the deformed powder samples occurred below the Curie temperature (630 K / 356°C). "Quenched" powders were created from the deformed + annealed powder by annealing at 850°C for 1 hour and quenching the sealed silica ampule containing the sample in water [31]. Microscopy and mechanical testing were performed on pieces of the ingot that were tempered under the same conditions. The mechanical test specimen was extracted from pieces of the bulk ingot of $MnCu_2Al$ using focused ion beam milling (FIB) for observation and analyses during the *in situ* micro-Laue compression tests, as previously described by Ref. [28]. FIB milling was performed using a TFS Helios NanoLab 600, operating at a voltage of 30 kV at various currents, and finished with a final ion polishing step at 5 kV, 16 pA to minimize FIB-induced damage.

Magnetic measurements were performed using a Quantum Design SQUID magnetic property measurement system equipped with a vibrating sample magnetometer. Magnetization was measured as a function of applied field at 5 K after cooling from ambient temperatures under zero applied field.

Synchrotron powder x-ray diffraction (XRD) data were collected on beamline 11-BM at the Advanced Photon Source,

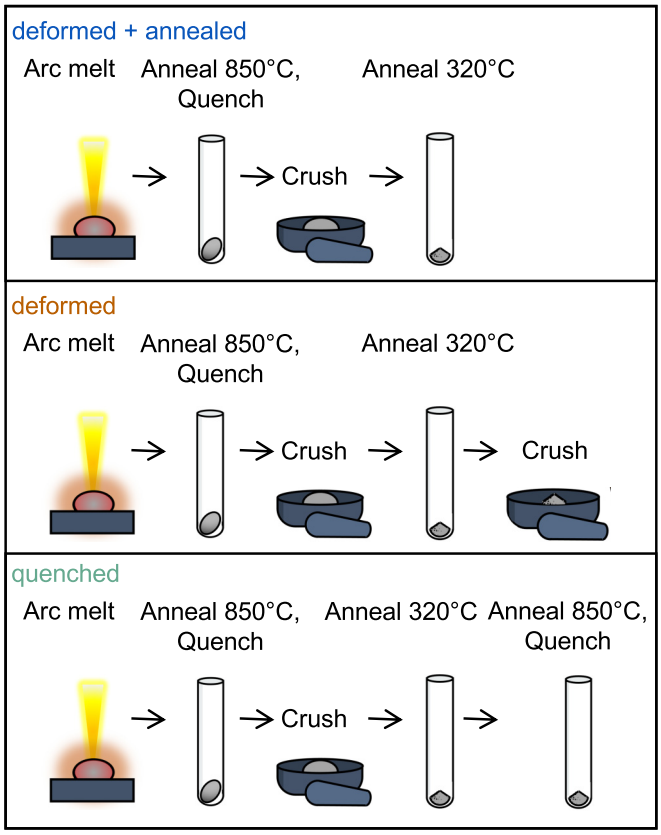

FIG. 2. Schematic of the processing routes used to prepare the $MnCu_2Al$ samples in the "deformed + annealed", "deformed", and "quenched" conditions. The presence of two additional peaks in the deformed diffraction pattern were investigated using scanning transmission electron microscope energy dispersive x-ray spectroscopy (STEM EDS) on a cross section of the particle and was determined to be a surface-adhered Si-O particle, likely originating from the agate mortar the powder was prepared in (see also Fig. S2 within the Supplemental Material [50]).

Argonne National Laboratory ($\lambda = 0.4589$ Å). Rietveld refinements [32] were performed on the resulting patterns using TOPAS ACADEMIC V7 [33]. Representations of the $L2_1$ structure were drawn using VESTA-3 [34]. Peak position (θ_{hkl}) and breadth (β_{hkl}) data were plotted in the form of Williamson-Hall plots [35–38], using an instrument resolution function characterized using the NIST Si 640d calibration specimen (600 μm), constants extracted from [28,39–44], and visualized using the batlow scientific color map [45]. The hyper surface of the $MnCu_2Al$ diffraction Young's modulus was generated, in part, using the ORIX Python package [46].

In situ microcompression testing on the micropillar (with dimensions of 5.7 μm×5.4 μm×9.0 μm), in combination with Laue microdiffraction, was performed using a FemtoTools FT-NMT04 nanoindenter equipped with a 10 μm diamond flat-punch [31]. The micropillar was loaded in a displacement-controlled mode with a displacement rate of 0.08 μm/s (strain rate of 0.0089 s^{-1}), up to significant plastic strains. Crystalline phase and crystal orientation were imaged during microcompression by *in situ* Laue microdiffraction. For this purpose, the FT-NMT04 nanoindenter was installed on the

xyz-sample stage of the BM32 beamline at the European Synchrotron ESRF in Grenoble (France). The sample plane is rotated by 40° with respect to the incident x-ray beam with the *x* axis oriented along the micropillar. The incident polychromatic x-ray beam with an energy bandwidth from 5 to 25 keV was focused down to 300 nm (H)×500 nm (V) using a pair of Kirkpatrick-Baez mirrors. The diffracted x-rays were recorded by a sCMOS (Photonic Science) detector with 2016×2018 pixels and a pixel size of 73.4 μm, which was installed at an angle of 90° with respect to the incident x-ray beam at a distance of 77 mm from the sample position. The Laue diffraction patterns were indexed by means of the open-source software packages LAUETOOLS [47] and LAUETOOLSNN [48] that have been developed by the beamline staff. The experimental geometry (sample-detector distance and the inclination and rotation of the detector) was calibrated using the Laue diffraction pattern of a Ge single crystal. This included a peak search, a manual preadjustment of the crystal orientation and geometry parameters by visual matching between the theoretical and experimental patterns followed by an automatic refinement of the orientation and the geometry. During *in situ* microcompression of the micropillars, Laue microdiffraction patterns were recorded at a single position of the micropillar with a 1 Hz rate. Postmortem Laue microdiffraction maps of the whole micropillar before and after microcompression were recorded by raster scans with steps of 300 nm.

A detailed microstructural investigation was performed on electron transparent foils micromachined from the powders and pressed specimen using FIB milling procedures as previously described. Local microstructural characterization was performed using an FEI Talos F200X TEM/STEM with ChemiSTEM EDS, operating at 200 kV in standard TEM operating mode, BF STEM mode, and STEM with EDS with a collection angle of 9 mrad. 4D-STEM data were collected using a Ceta-M detector on an FEI Talos F200X TEM/STEM using a convergence angle of 0.6 mrad and a camera length of 0.125 m. Processing of the 4D-STEM data and construction of the orientation maps was performed using the PY4DSTEM Python package [49] (see Sec. S5 of the Supplemental Material [50]), with further analysis of the orientation maps performed using EDAX OIM Analysis. DPC STEM was collected using a TFS segmented BF detector on an FEI Talos F200X TEM/STEM. Alignments were performed to tune the objective lens to 0%, resulting in an applied field of 0.01220 T –0.01077 T, and a convergence angle of 0.15 mrad. Additional alignments were performed to tune the objective lens to 93.8%, resulting in an applied field strength of 2.2 T. Hall probe measurements of the magnetic field *in situ* in the TEM are found to scale linearly with objective lens strength. The single crystalline specimen was tilted off zone (10°) to suppress diffraction contrast while imaging to avoid strongly exciting Bragg conditions.

All DFT calculations were performed within the Vienna *Ab initio* Simulation Package (VASP) [51] using projector-augmented-wave (PAW) pseudopotentials [52,53] within the Perdew-Burke-Ernzerhof (PBE) generalized gradient approximation (GGA) [54] with a plane-wave energy cutoff of 500 eV. A Monkhorst-Pack scheme was used to construct the Brillouin zone [55] and spin polarization was also included. The magnetic moments of Mn, Cu, and Al were initialized with magnitudes of 4 μ_B, 0.5 μ_B, and 0.5 μ_B, respectively. γ surface calculations were performed on supercells generated *via* the software package MULTISHIFTER [56]. Specifically, the {110} γ surface was sampled by a 15×21 grid along the [110] and [001] directions, respectively, with the total number of calculations then being further reduced by the mirror symmetries present within the $L2_1$ crystal structure. Periodic images of the planar faults were separated by greater than 16 Å and only structural relaxation normal to the plane of the fault was allowed. To elucidate the effect of magnetic ordering on the fault energies, the energy of each atomic configuration of the γ surface was calculated with both a ferromagnetic and an antiferromagnetic coupling across the fault, where for the antiferromagnetic configurations the magnetic moments of the Mn atoms above the fault were assumed to point antiparallel to the magnetic moment of the Mn atoms below the fault. As a result, two γ surfaces were calculated and will be referred to as a "ferromagnetic γ surface" and "antiferromagnetic γ surface." Both sets of computed energies are then used to fit Fourier series of the form

$$E^{\gamma}(\Delta_{001}, \Delta_{110}) = \Sigma_n \Sigma_m A_{nm} \cos\left(\frac{2\pi n \Delta_{001}}{a_0} + \frac{2\pi m \Delta_{110}}{\sqrt{2} a_0}\right), \tag{2}$$

where a_0 is the lattice parameter of $MnCu_2Al$ determined from DFT, Δ_{001} is the shear displacement along the [001] direction and Δ_{110} is the shear displacement along the [110] direction, both relative to the unfaulted crystal. All ferromagnetic supercell calculations contained 32 atoms per cell, while the antiferromagnetic supercell calculations contained 64 atoms per cell.

III. RESULTS

A. Dramatic impact of plastic deformation on macroscopic magnetic properties in $MnCu_2Al$

We first investigate the impact of processing conditions that are known to induce high densities of planar defects on the macroscopic magnetic properties of $MnCu_2Al$. Magnetic hysteresis curves of the $MnCu_2Al$ powders reveal a dramatic difference in their magnetic properties, depending on their treatment [Fig. 1(b)]. The deformed + annealed response is representative of the S-shaped curve of a ferromagnet and has $M_s = 3.74\ \mu_B$. The quenched powder is also reminiscent of the S-shaped curve of a ferromagnet but with a reduced M_s of 3.11 μ_B. Measurements of the deformed sample, in contrast, are not consistent with the magnetic response of a conventional ferromagnet. The saturation magnetization was found to be 0.172 μ_B using approach-to-saturation fits [57–61] applied to the deformed sample magnetization curve (see Sec. S1 of the Supplemental Material [50]), which would correspond to a 95.4% decrease from the M_s of the deformed + annealed state. The magnetization never fully saturates and appears nearly linear, except in the low-field limit. This magnetic response is consistent with a composite magnetic response between a large volume fraction of antiferromagnetic regions hosted within a ferromagnetic matrix.

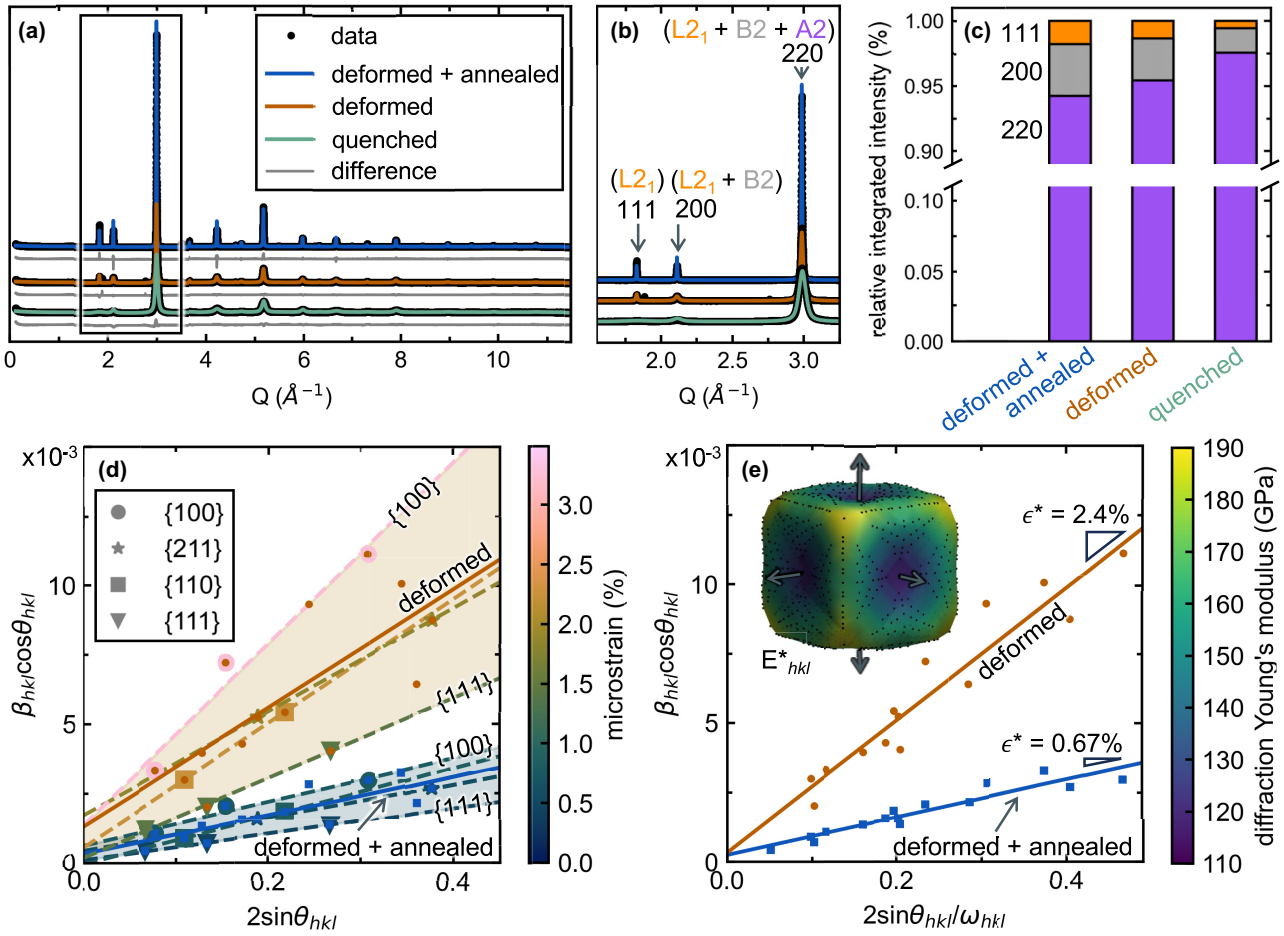

FIG. 3. (a), (b) Rietveld refinements of the synchrotron powder x-ray diffraction patterns of $MnCu_2Al$ powders in the deformed + annealed, deformed, and quenched conditions. (a) Full diffraction patterns and (b) enlarged view of the 111, 200, and 220 peaks indicated by the black box in (a) to emphasize differences in intensities and peak broadening between the different powder samples. (c) Bar chart of the integrated intensities of the 111, 200, and 220 peaks relative to one another for each powder sample. (d) Conventional Williamson-Hall plot and (e) direct-fit Williamson-Hall plot of the deformed + annealed and deformed diffraction patterns, indicating an orientation dependence of microstrain among different $\{hkl\}$ families of planes. In (d), solid lines indicate the average Williamson-Hall fit of each powder sample, while the dashed lines indicate the Williamson-Hall fits of $\{hkl\}$ families. The {111} and {100} families bound the spread of points for each powder sample, respectively. The dispersion is corrected in the direct-fit Williamson-Hall plot in (e). The hypersurface of the $MnCu_2Al$ diffraction Young's modulus (E^*_{hkl}) used in the ω_{hkl} parameter of (e) is inset.

The magnitude of the reduction in M_s due to deformation of $MnCu_2Al$ appears to be higher than reported for any $L2_1$-ordered intermetallic [17–25], excluding cases exhibiting phase changes via transformation induced plasticity. Changes to magnetization in the high-field limit typically can be attributed to fundamental differences in the magnetic coupling interactions of the samples, rather than to magnetization processes through domain wall motion and domain rotation [62,63]. Previous investigations within Mn-based $L2_1$-ordered intermetallics have attributed decreases in M_s to the formation of extended antiphase boundaries generated either through plastic deformation or quenching, resulting in a composite magnetic response between the antiferromagnetic regions hosted by the defects and the remaining ferromagnetic matrix. $MnCu_2Al$ has been shown to be capable of deforming to greater than 20% plastic strain [64], showing that it has a high capacity for forming defects through plastic deformation. If an antiferromagnetically coupled volume of material hosted by the planar defects is responsible for the observed composite magnetic response, the observed magnitude of reduction in M_s would require that a large fraction of the volume of material in the deformed sample be antiferromagnetically coupled [16–18,22,65]. Alternatively, a phase change induced by the deformation, or antisite disorder to the nonmagnetic $A2$ or $B2$ structures could achieve a similar result. While the M–H measurements highlight the suppression of macroscopic M_s, either by quenching or plastic deformation, the comparative impact of chemical order and defect densities present in the powders needs to be resolved.

B. Quantification of the extent of macroscopic chemical disorder and defect densities induced by plastic deformation

We next assess the identity of phases and the degree of chemical order present in each of the powder samples using Rietveld refinements of synchrotron powder XRD patterns [Fig. 3(a)]. Each sample was found to be representative of a single phase in the $Fm\bar{3}m$ space group, with the $MnCu_2Al$ $L2_1$

crystal structure. A notable difference between the diffraction patterns can be detected in the relative intensities of the first three measured diffraction peaks, which can be used to assess antisite disorder in the $L2_1$ structure [Fig. 3(b)]. In a $L2_1$ diffraction pattern, the 111 peak is exclusive to the $L2_1$ structure. The 200 peak can contain contributions from both the $L2_1$ and disordered $B2$ structure, while the 220 peak can contain contributions from the $L2_1$, $B2$, and $A2$ structures. In the deformed + annealed sample, the Rietveld fit of the $L2_1$ structure fits well to the measured intensities, indicating that the sample is fully ordered in the $L2_1$ structure. However, in the quenched sample's diffraction pattern, the integrated intensities of the 111 and 200 peaks have reduced in comparison to the 220 peak by ≈20% [Fig. 3(c)]. This shows that the quenched sample has retained approximately 20% more $A2$-type antisite disorder from the high-temperature treatment than in a fully ordered $L2_1$ crystal. In the quenched sample, the difference in ordering could explain the observed reduction in M_s.

The deformed sample's diffraction pattern, which corresponds to a dramatically larger reduction in M_s, fits very well to the Rietveld peak intensities, suggesting that it has a negligible amount of antisite disorder within the bulk of the crystal. Thus, the primary mechanisms responsible for the reduction in M_s in the quenched and deformed samples are of fundamentally different origins.

In samples subjected to severe plastic deformation, such as in the deformed powder, dislocations and subsequent grain boundaries that may form during plastic sub-grain formation or grain fragmentation processes [66–68] are the primary defects expected to be generated, since widespread cracking is not observed [69]. Correspondingly, small coherently diffracting domain sizes (D_{vol}) and nonuniform microstrains induced by dislocations (ϵ^*) both serve to increase the XRD peak breadths, and can be independently quantified using Williamson-Hall plots in fully ordered materials [Figs. 3(d) and 3(e)]. A direct-fit Williamson-Hall [37] more accurately captures the average D_{vol} and ϵ^* of each sample by normalizing the strain anisotropies owing to defects, using the diffraction Young's modulus ratio $\omega_{hkl} = E^*_{hkl}/E_0$ [inset of Fig. 3(e)], which can be calculated using the $MnCu_2Al$ elastic constants [39] (see more details of these calculation in Appendix A). The coherently diffracting domain sizes of the deformed + annealed and deformed samples suggest nanoscale crystallite sizes, slightly increasing from 139 nm to 185 nm with the annealing treatment. Dislocation cell structures and subgrain boundaries are thought to contribute to coherently diffracting domain dependent peak broadening in addition to grain boundaries [70,71].

Microstrains are nonuniform distributions in interplanar spacings, which generally accompany the presence of dislocations and planar defect structures [35,42]. In the direct-fit Williamson-Hall plot in Fig. 3(e), the average microstrain increases by a factor of $3.5x$ (from $\epsilon^* = 0.67\%$ to $\epsilon^* = 2.4\%$) after deformation, which can be attributed to a general increase in defect density [36]. Using the modified Williamson-Hall approach [36], the magnitude and anisotropies in ϵ^*, shown in Fig. 3(e), were used to quantify defect densities in both states (see Appendix A). Using this method, the defect density in the deformed + annealed sample was found to be 7.7×10^{15} m^{-2}, which increased to 2.6×10^{16} m^{-2} after deformation. As is generally expected of defect densities generated using fits to x-ray diffraction data, the quantitative values are not expected to be reliable but should be qualitatively correct in relation between datasets. The primary source of peak broadening for both of these samples can be attributed to microstrains induced by dislocations.

C. Defect-mediated microstructural refinement and recrystallization

To reveal the nanoscale mechanisms underlying the control over magnetic properties in this intermetallic, we probed the deformation microstructures in the interior regions of the powder particles that had been both deformed and deformed + annealed using scanning electron nanodiffraction (also known as 4D-STEM [72]). Directly following plastic deformation, $MnCu_2Al$ has maintained its initially large-grained microstructure [Figs. 4(a) and 4(c)] but is punctuated by boundary traces that are consistent with either true- or pseudo-nanotwins of the ⟨111⟩{112} type, which occur in systems exhibiting slip of the ⟨111⟩{110} or ⟨111⟩{112} type [30]. The twinned orientations make up an estimated ≈11% area fraction shown in the field of view of Fig. 4(c), but are found with at least 50% lower frequency throughout the larger specimen (see Fig. S3 within the Supplemental Material [50]). As a result, we estimate that the twinned regions account for no more than ≈5% of the volume of the powder sample. Twinning in systems that exhibit slip through planar defect structures typically does not occur unless substantial plastic deformation through slip has been recorded [73,74], implicating the presence of a large population of intragranular defects. The spatially averaged diffraction pattern (SADP) [Fig. 4(d)] supports this hypothesis by showing that the crystalline orientation of Figs. 4(a) and 4(c) is primarily representative of a single mean orientation, albeit with spatially varying misorientations characteristic of accumulated plastic slip and/or twinning. This is reflected in the broad distribution of kernal average misorientations (KAM) measured within the frame of view [Fig. 4(g)], suggesting a strong link to a large population of intragranular extended dislocation structures that induce the observed lattice rotations. The misorientation peak at 60° ± 2.5° corresponds to the 60° rotation about the ⟨111⟩ axis observed at the boundaries of the ⟨111⟩{112} twins [Fig. 4(h)] [30,73,75,76]. The low misorientation tail relates to the increasingly random distribution of crystal rotations, which can be explained by rotational modes operative during severe plastic deformation through the motion and interactions of dislocations that precedes organization into dislocation cell walls and/or low-angle subgrain boundaries [77,78].

After annealing [Figs. 4(b) and 4(e)], the grain structure has evolved toward smaller grains with unique orientations. This is evident in the SADP [Fig. 4(f)], which shows the presence of a variety of crystalline orientations that have recrystallized from the prior deformed state. The narrow distribution of KAM within a single grain [indicated in Fig. 4(i)] indicates a decreased density of defects within the bounds of recrystallized grains. After annealing, the misorientation distribution [Fig. 4(j)] shifts to represent a Mackenzie-like quasirandom distribution of high-angle boundaries [79]. The

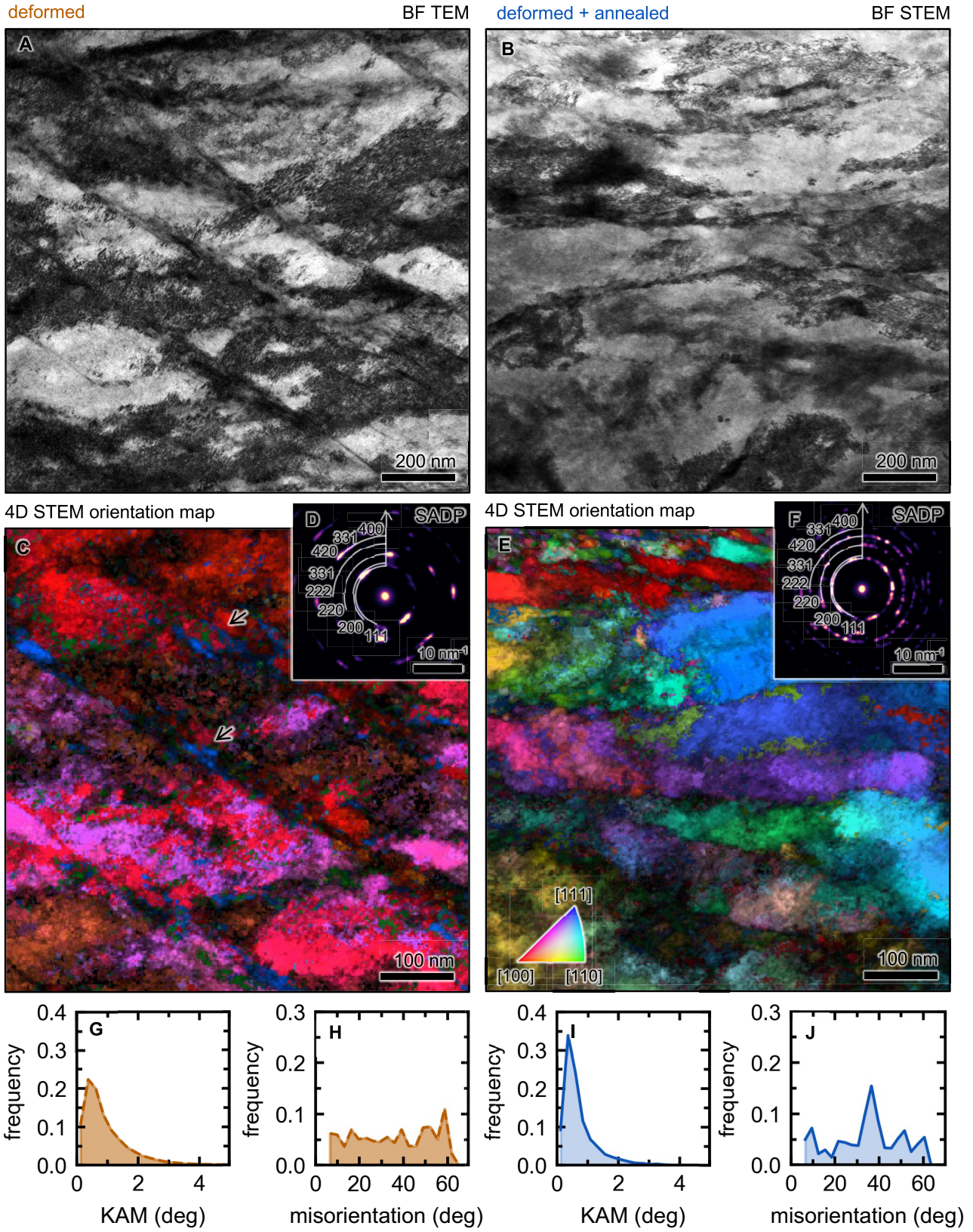

FIG. 4. (a) Bright field transmission electron microscopy (BF TEM) micrograph of the deformed $MnCu_2Al$ and (b) scanning transmission electron microscopy (STEM) micrograph of the deformed + annealed $MnCu_2Al$ samples. (c) 4D STEM orientation map, and (d) spatially averaged diffraction pattern (SADP) of the deformed powder. Orientation maps are colored using the FCC inverse pole figure (IPF) triangle inset in (e). Arrows in (c) indicate the position of localized slip. (e) 4D STEM orientation map, and (f) SADP of the deformed + annealed powder. (g) Frequency vs kernal average misorientation (KAM, degree) and (h) frequency vs misorientation within (c). (i) Frequency vs kernal average misorientation (KAM, degree) and (j) frequency vs misorientation within (e).

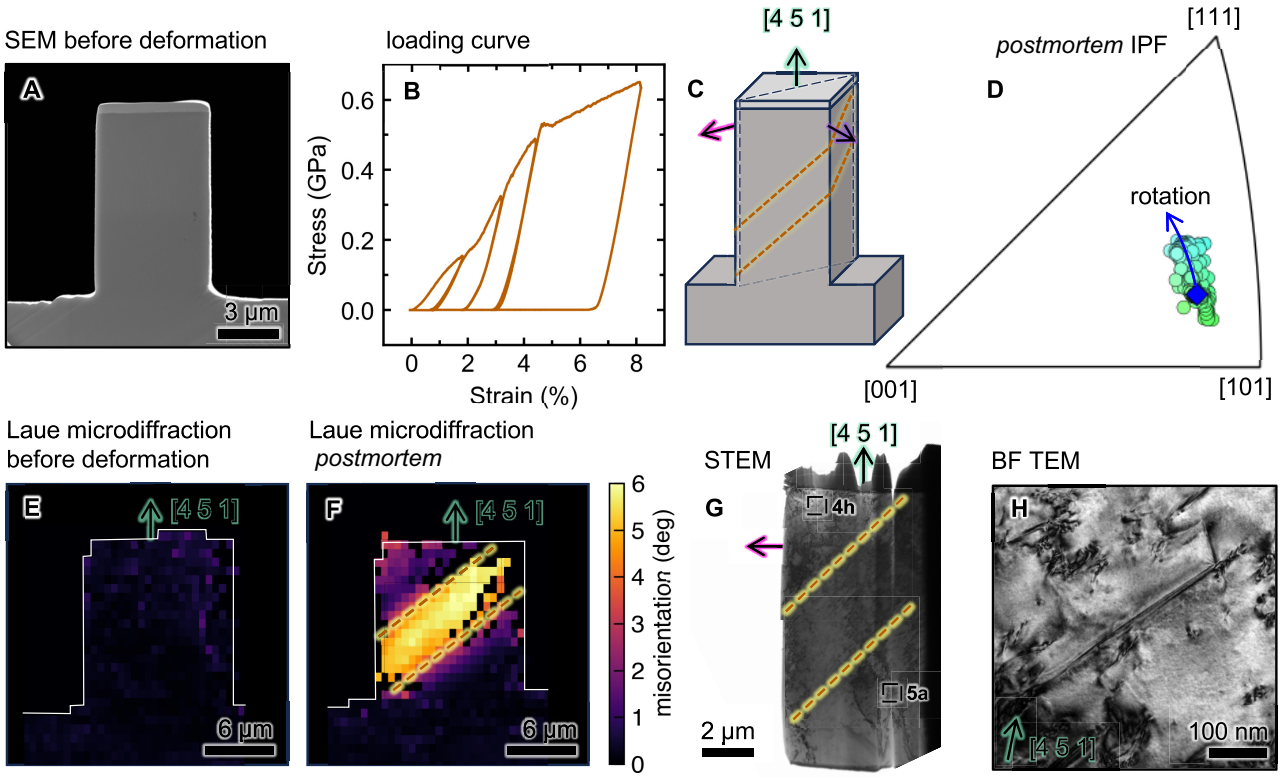

FIG. 5. (a) Scanning electron microscopy (SEM) micrograph of undeformed $MnCu_2Al$ microcompression pillar prepared through micromachining with focused ion beam milling. (b) Stress vs strain data acquired during the compression of the micropillar *in situ* in a synchrotron micro-Laue beamline. The pillar was loaded and unloaded multiple times and was not deformed to the point of failure to preserve the defect structures resulting from deformation. (c) Schematic of the micropillar, indicating the compression axis and orientation of Laue microdiffraction mapping. (d) FCC inverse pole figure showing crystalline rotation of the pillar around the pillar compression axis because of deformation of slip planes. (e), (f) Micro-Laue misorientation plots relative to the average orientation along the pillar compression axis ([451]) collected (e) before and (f) after deformation of the micropillar, showing the localization of slip. The pillar boundaries are indicated with white outlines for clarity. (g) A bright field scanning transmission electron microscope (BF STEM) micrograph of the lamella pulled from the deformed pillar. (h) BF transmission electron microscopy (TEM) micrograph from the defects resulting from deformation.

peak near 40° appears to correspond to the Σ5 ⟨001⟩ symmetric tilt boundary expected in bcc-derived materials ($\theta = 36.87°$) [80–82]. These crystallographic orientation statistics are consistent with a recrystallization process promoted by the driving force from the stored elastic energy of the dislocation population introduced via deformation. In neither sample were we able to resolve individual defect structures or dislocations because of the ultrahigh defect density and associated high degree of crystallographic heterogeneity caused by deformation, consistent with the high defect densities estimated from the XRD analysis shown in Fig. 3. The high contrast originating from orientation contrast (and presumably from the high defect density) prohibited any direct quantification of the defect density directly from the TEM data.

D. Defect-level role of deformation in controlling macroscopic magnetic properties

To elucidate the origins of the magnetoplastic effect observed in $MnCu_2Al$ at the single defect level, we employed micromechanical testing of a single crystal in the [451] loading orientation, and introduced smaller amounts of plastic strain [Fig. 5(a)] and used micro-Laue diffraction mapping to quantify ensuing lattice rotations. The expected slip for this orientation via Schmid analysis is on the $[11\bar{1}](011)$ system when loaded in uniaxial compression. After deformation to significant plastic strains [Fig. 5(b)], regions of the pillar were seen to rotate away from the initial crystallographic orientation [Fig. 5(d)], indicating deformation through plastic slip on crystallographic planes [83]. This is supported by the observation that before deformation, the misorientation from the mean orientation is seen to be low, indicating a high crystalline quality of the sample [Fig. 5(e)]. After deformation, the misorientation with respect to the initial orientation increased, and is seen to be localized within a single large slip band, indicated by dashed lines [Fig. 5(f)]. This suggests that defects within this region of the pillar are primarily the product of deformation-induced crystallographic slip, rather than a preexisting population of defects introduced through processing. This facilitates a study directly correlating deformation-induced defects to corresponding magnetic signatures.

A TEM lamella was extracted from the deformed pillar with an orientation normal to the projection of the Laue maps, and was found to contain a dense population of defects within the bounds of the slip band identified through the micro-Laue maps. A representative defect structure from this

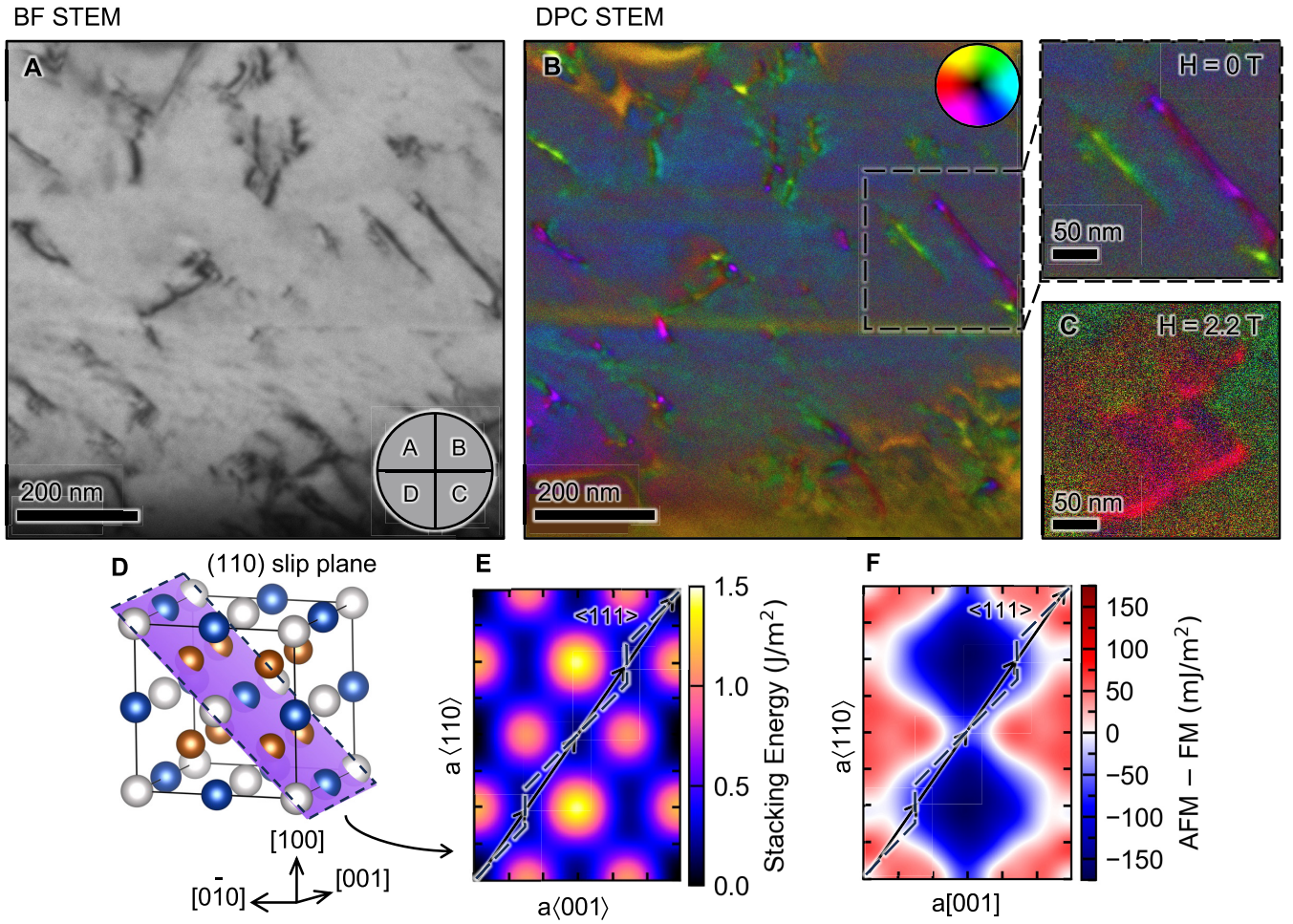

FIG. 6. (a) Bright field scanning transmission electron microscope (BF STEM) micrograph collected from a segmented detector of the $MnCu_2Al$ specimen (schematic inset). (b) Differential phase contrast (DPC) STEM micrograph corresponding to the segmented BF STEM micrograph in (a), collected with zero applied field (applied by the objective lens). The DPC maps are colored using the direction of the in-plane induction indicated by the inset color wheel. An enlarged view of the defects is positioned to the right. The inset color wheel maps the in-plane magnetic induction to colors. (c) DPC STEM micrograph of defects collected with an applied field of $H = 2.2$ T. (d) The $MnCu_2Al$ unit cell, depicting a {110} slip plane. (e) γ-energy surface and (f) magnetic configuration map of the {110} plane, overlaid with the dissociation pathway observed for the screw (solid) and edge (dashed) defects in $MnCu_2Al$ in our previous investigation [28].

region was characterized by moving slightly above the deformation band to the region indicated by the box in Fig. 5(g) [shown in Fig. 5(h)]. The contrast observed may suggest the presence of a stacking fault or antiphase boundary, though the characteristic antiphase contrast was not detected because of the large extinction distances that are present in several $L2_1$-ordered intermetallics [23,28]. The slip characteristics of the dislocations are otherwise consistent with the planar dissociation of a full dislocation into partial dislocations bounded by planar faults in $MnCu_2Al$ [17,26,28], with a reaction following via Eq. (1) or

$$[111] = b_1 + b_2 + b_1 + b_1 + b_2 + b_1, \tag{3}$$

where $b_1 = \frac{1}{4}[\alpha, \alpha, 1]$, $b_2 = \frac{1}{2}(1-\alpha)[1, 1, 0]$, and $\alpha \approx \frac{3}{4}$ for $MnCu_2Al$ [28]. We next investigate whether defects introduced by deformation can host unique magnetic properties, as predicted by [17–25], compared with the pristine matrix.

Defect-level characterization of the magnetic induction in the vicinity of the deformation-induced defects was accomplished using differential phase contrast (DPC) STEM, collected using a segmented bright field (BF) detector to facilitate spatial mapping of the in-plane magnetic induction both near and away from the defects. Importantly, these measurements were performed in both near-zero field and high field ($H = 2.2$ T) environments to determine whether any magnetic signatures are related to intrinsic spin characteristics at the defects or a result of domain pinning behavior. Representative individual defect structures were identified by moving slightly below the deformation band to the region indicated by the box in Fig. 5(g). A micrograph collected by one segment of the detector is shown in Fig. 6(a), along with a schematic of the detector geometry. The DPC STEM image generated from these micrographs is shown in Fig. 6(b) and is colored using the direction of the in-plane induction indicated by the inset color wheel. The DPC STEM image shows a single ferromagnetic domain spanning the mapped region with the resolved in-plane induction oriented toward the bottom right corner of the image, which is interrupted by ribbon-like regions of induction that coincide with the position of the defects observed in Fig. 6(a). The DPC STEM

induction map does not show the presence of any defined magnetic domain walls, whereupon a 180° change in induction orientation would occur (blue to yellow). In contrast, the defect structures present in the field of view show a pronounced and localized change in induction and intensity, indicating that the magnetic environment bounded by the planar defects is different from that of the surrounding ferromagnetic material.

The contrast in this region occurs as a result of the integrated magnetic induction along the path of the electron beam and through the inclined planar defects bounded by partial dislocations. Notably, the induction present on either side of the defects appears to be largely unaltered, indicating that the encompassing ferromagnetic domain is not impacted by the magnetic features present at the defect structures. At an applied field of $H = 2.2$ T [Fig. 6(c)], these features persist at the location of defect structures and have not magnetized in the same direction as the encompassing ferromagnetic domain, which is presumably in the direction of the in-plane field induced by the objective lens. This suggests that the material in the direct vicinity of the defects is not ferromagnetic in origin. We next discuss how the observed induction modulation is consistent with a narrow ribbon of material with differing magnetic coupling than the surrounding matrix.

IV. DISCUSSION

In Sec. III A, we have shown that an increasing defect density is associated with a dramatic decrease in the magnetization across a large range of field strengths, as well as a change in the magnetic induction surrounding planar defect structures introduced through plastic deformation. Remarkably, this change in macroscopic magnetic response is the result of plastic deformation while preserving the overall ordering of the $L2_1$ phase, and is reversible following heat treatments that promote recrystallization to lower the defect density (Secs. III B and III C). In the following discussion, we link these two observations by characterizing the magnetic environment surrounding planar defects as antiferromagnetic through DFT calculations, and rationalize the macroscopic observations by estimating the fraction of material affected by the presence of defects.

Our experiments show a correlation between the dramatic decrease in M_s, the formation of defects, and the presence of unique magnetic induction surrounding planar defects. The resulting M–H curve of the deformed sample suggests that the material has either developed new magnetic exchange interactions because of the plastic deformation imparted onto the sample, or alternatively, that the ferromagnetic domains are pinned by the defects formed during plastic deformation and are unable to fully align under an applied field of 7 T. The "approach to saturation" fits applied to both samples confirm a lower saturation magnetization is indeed expected for the "deformed" sample (see the Supplemental Material [50]). Given the magnitude of the reduction in magnetization at 7 T, we would expect that if this sample is ferromagnetic, domain pinning would be a prominent effect observable by local magnetic imaging. We eliminate this as a possibility by locally imaging the magnetic domain configurations present in the material using differential phase contrast (DPC) STEM at room temperature. Importantly, the magnetic domains in our micrographs do not appear to be pinned, demonstrating that magnetic domain pinning is not a likely contributor to the decrease in magnetization at 7 T. Instead, there is contrast present at the planar defects that is most consistent with a twisted strip of antiferromagnetic character. In light of these observations, we hypothesize that differences in M_s between the deformed sample and the deformed + annealed sample are linked to local structural features of the material, rather than rate-dependent mechanisms, such as domain wall pinning or domain rotation that would be more likely to affect coercivity. We observed that the $L2_1$ phase ordering is retained in the deformed sample and in the deformed + annealed sample, though the macroscopic magnetic properties of the powders are drastically different. The TEM observations of the microstructures show that a large-grained microstructure from the arc-melted button (prior to deformation) has been retained in the deformed sample. There is evidence of slip-like characteristics in the TEM micrographs that are associated with the passage of a high density of slip-mediating defects, consistent with XRD results indicating a very high density of defects in the deformed sample of 2.6×10^{16} m^{-2}. In the deformed + annealed sample, $MnCu_2Al$ shows a homogeneous small-grained microstructure. These nanoscale grains have presumably recrystallized from the large-grained yet heavily deformed microstructure comprising the deformed sample, because of the driving force for recrystallization associated with the rearrangement or elimination of defects ($\Delta E \propto \rho G b^2$, where ρ is dislocation density, G is the shear modulus, and b is the Burgers vector magnitude) [84]. Through this process, the grains with high densities of defects eradicate their defect content by the nucleation of new grains to reduce the stored strain energy [18,84,85]. Consequently, the global defect density is reduced to 7.7×10^{15} m^{-2}. The formation of new grains with relatively low intergranular defect densities introduces high angle grain boundaries that could pin magnetic domain boundaries [23,86], reducing the rate of magnetization processes at low applied magnetic fields ($H < 1$ T), thus increasing the coercivity. However, this phenomenon cannot account for our observed decrease in M_s ($H = 7$ T), where all domains have magnetized and the measured magnetization is representative of the strength of ferromagnetic coupling within the material rather than the rate of magnetization. The TEM and XRD results support this, as the average coherently diffracting domain size remains relatively constant following the anneal step. The observed defects [Fig. 6(a)] are consistent with the $\langle 111\rangle\{110\}$ defects typically observed upon deformation of $L2_1$-ordered intermetallics, although the potential dislocation dissociation and the resulting planar faults bounded by partial dislocations are not detected because of the large extinction distances. Thus, it can be assumed that differences in the M_s are primarily related to the defect densities, rather than other microstructural features such as grain boundaries.

The DPC STEM magnetic induction maps of the dislocation structures show contrasting features that can be associated with the presence of antiferromagnetic strips separating the abutting regions of identically magnetized material. The $\langle 100\rangle\{100\}$-type antiphase boundaries generated by quenching $MnCu_2Al$ [18] and in $MnNi_2Ga$ [23]

and by deforming $MnCu_2Al$ [17] in prior work have been observed to pin oppositely magnetized regions of material. The antiphase boundaries have been argued to act as a nonmagnetic strip that is attributed to a possible antiferromagnetic interaction between Mn atoms that locally resemble the nonmagnetic $B2$ structure [16–18,23]. Venkateswaran *et al.* showed that the magnetic induction across quenching defects in $MnNi_2Ga$ does not change direction unless the quenching defects coincide with 180° domain walls [23]. Via simulation, they showed that the expected contrast from a twisted thin strip of zero net magnetic induction separating two regions of identically magnetized material can be fully explained by antiferromagnetically coupled antiphase boundaries inclined within a single ferromagnetic domain. In a defocus Fresnel image series, the expected contrast produced an alternating black and white contrast bounding the antiferromagnetic strip. When integrated into an induction color map, such as our DPC STEM micrographs, the contrast showed either no induction when the antiferromagnetic strip was parallel to the imaging direction, or showed a local change in the color intensity when inclined with respect to the imaging direction, though the direction of induction within the surrounding domain was unaltered. Their simulations are in good agreement with our DPC STEM induction maps, supporting the presence of an antiferromagnetic strip at the planar defects within the dissociated dislocation. Notably, an increase in the applied magnetic field would not be expected to impact the induction observed surrounding the defects hosting a local antiferromagnetic environment, since it cannot be magnetized by an increasing applied field. This is consistent with our observations that the magnetic contrast hosted by the defect structures persists at an applied field of 2.2 T [Fig. 6(c)].

In order to probe the expected local magnetic order exhibited by the ⟨111⟩{110}-type planar defects found within $MnCu_2Al$, we perform γ surface calculations based on density functional theory to resolve how particular shear displacements within a {110} plane may promote either ferromagnetic or antiferromagnetic coupling across a generalized stacking fault. Figure 6(e) shows the resulting γ surface when only ferromagnetic coupling across the generalized stacking faults is considered, as was the case in our previous investigation [28]. However, when calculations assuming antiferromagnetic coupling across the fault are considered, shear displacements that correspond to large atomic displacements (like those found across antiphase boundaries) are lower in energy than their ferromagnetic equivalents. This fact is demonstrated clearly in Fig. 6(f), where it can be seen that all minima present within Fig. 6(e), while remaining in the same locations within Fig. 6(f), are lower in energy (by up to 64 mJ m^{-2}) when antiferromagnetic coupling is considered. The expected dissociation mechanisms of both screw and edge ⟨111⟩{110} dislocations computed by Rhodes *et al.* [28] are therefore still likely [shown in Figs. 7(a)–7(c)]; however, by considering the influence of the magnetic degree of freedom upon the energetics of the γ surface, we assert that the planar defect structures within the extended (dissociated) dislocations in $MnCu_2Al$ [28] host local antiferromagnetic order that is distinct from the ferromagnetic ordering expected for the bulk material. This is crucial because, as can be seen within Fig. 6(f), small lattice displacements—like those expected for the elastic strain fields surrounding an undissociated dislocation core—preserve the ferromagnetic order of the pristine lattice. Our work therefore reveals an exciting avenue for magnetoplastic control to be realized in Mn-based $L2_1$-ordered intermetallics (and potentially in any metallic material exhibiting both RKKY coupling and extended planar defect structures), when the density of extended planar defects is sufficiently high.

The degree to which the volume of planar defects predicted by Rhodes *et al.* [28] [shown in Figs. 7(a)–7(c)] may impact M_s can be estimated following the method proposed by Ikeda and Takahashi [19] (see Appendix B for complete details). In applying their formulation, we first assume here that the volume fraction of material associated with the spatially extended defects in both the deformed + annealed and the deformed powder, denoted as $\bar{V}$, may be treated as a function of the total dislocation density ρ, extracted by the modified Williamson-Hall fit. For simplicity, we assume that (i) the experimentally measured dislocation density is predominantly caused by ⟨111⟩{110} dislocations, and (ii) each of these ⟨111⟩{110} dislocations has dissociated into four $\frac{1}{4}$⟨111⟩{110} partials, which bound two symmetrically distinct faults,

$$[111] = b_1 + \text{Fault}_\text{I} + b_1 + \text{Fault}_\text{II} + b_1 + \text{Fault}_\text{I} + b_1. \tag{4}$$

As schematically shown in Fig. 7(e), the configuration of these faulted dislocations may then be assumed to occur as ribbons of antiferromagnetic material spanning n adjacent slip planes. Taken together, we may then express $\bar{V}$ as a function of n, the lattice parameter, a_0, and ρ as

$$\bar{V}(n, a_0, \rho) = \frac{na_0}{4\sqrt{2}}\rho[2w_\text{I}(\rho) + w_\text{II}(\rho)]. \tag{5}$$

This leads to the following expression for the fractional decrease in saturation magnetization relative to the pristine, dislocation free, saturation magnetization (a complete derivation is provided within Appendix B),

$$\frac{\Delta M_s}{M_s^0}(n, a_0, \rho) = -\frac{na_0}{2\sqrt{2}}[2\rho w_\text{I}(\rho) + \rho w_\text{II}(\rho)]. \tag{6}$$

Equation (6) requires the mean fault widths, w_I, and w_II, for fault I and fault II, respectively, to be determined. Generally speaking, these fault widths correspond to the average spacing between partials caused by the exact dislocation configuration of the sample. Setting $w_\text{I} = w_\text{II} = \frac{1}{\sqrt{\rho}}$ was an essential assumption for Ikeda and Takahashi to proceed further, as there was no other straightforward way at the time for them to infer mean fault widths. These defect configurations are discussed in further detail in Appendix B [shown schematically in Fig. 7(e)]. However, it is more likely that the partials will remain well separated, and perhaps even closely resemble a weighted average over the fault widths predicted for long, straight, dislocations. In particular, since the modified Williamson-Hall fit extracts the fraction S of dislocations expected to be of screw character, we may assume that w_I and w_II correspond to an average over the edge and screw fault widths predicted for long, straight, dislocations in $MnCu_2Al$, as previously determined by the phase-field dislocation

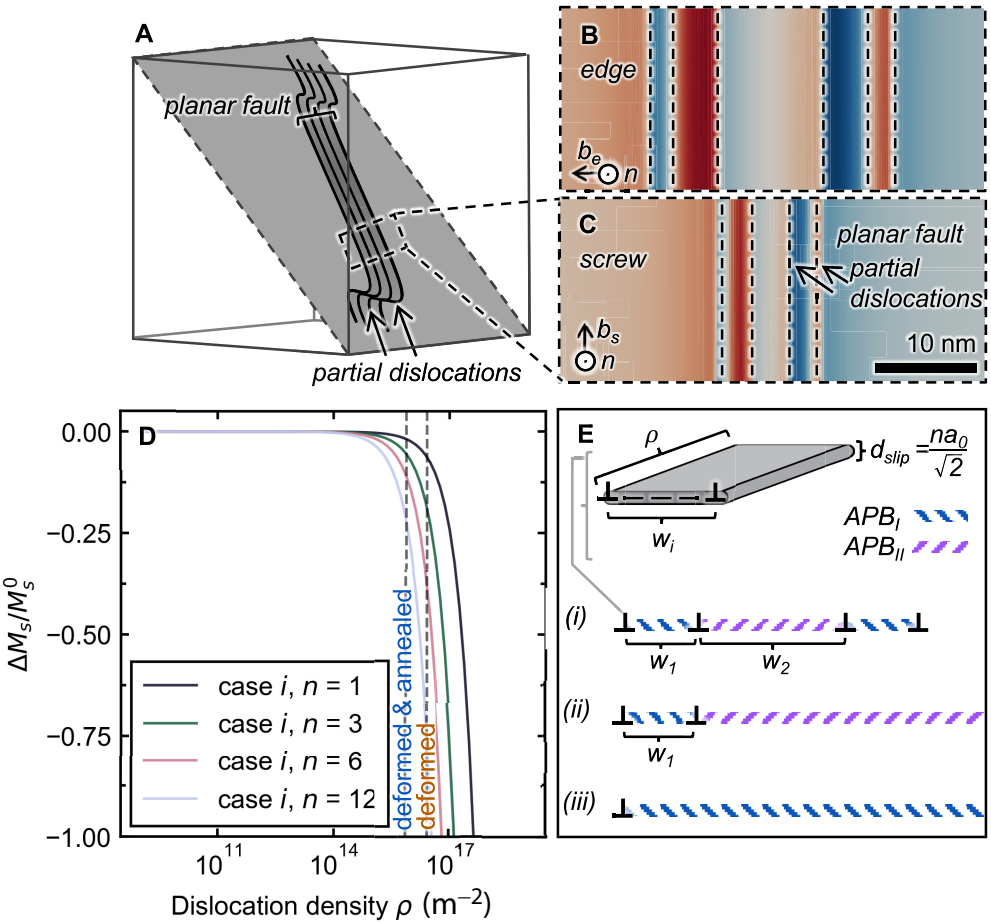

FIG. 7. (a) Schematic of planar faults in $MnCu_2Al$ imaged in projection using transmission electron microscopy. (b), (c) Simulated equilibrium configuration of the ⟨111⟩ defect structures with (b) edge and (c) screw character performed by Rhodes *et al.* [28]. The partial dislocations are indicated by dashed lines. (d) Change in M_s with increasing planar defect densities. (e) Schematic used to approximate the antiferromagnetic volume of material impacted by the planar defects. Cases (ii) and (iii) are discussed in Appendix B for completeness.

dynamics simulations of Rhodes *et al.* [28] and summarized in Fig. 7(b). w_{I} and w_{II} may then be expressed as

$$w_i = (1 - S)w_i^e + Sw_i^s, \tag{7}$$

where w_i^e and w_i^s are the calculated edge and screw fault widths for the ith fault, by way of the phase-field approach. Specifically, $w_{\mathrm{I}}^e = 7.5$ nm, $w_{\mathrm{II}}^e = 10$ nm, $w_{\mathrm{I}}^s = 3$ nm, and $w_{\mathrm{II}}^s = 4$ nm.

Upon inserting, Eq. (7) into Eq. (6), $\frac{\Delta M_s}{M_s^0}$ may now be plotted in Fig. 6(d), along with the dislocation densities measured for the deformed + annealed and deformed sample of $MnCu_2Al$. Rather remarkably, this model demonstrates that the observed experimental change in dislocation density is indeed of an order of magnitude that could lead to the major decrease in the saturation magnetization that has been observed experimentally. Additionally, the model indicates that the faulted ribbon must span beyond one adjacent slip plane to reconcile our experimental findings. It is also worth noting that the saturation magnetization of "pristine" $MnCu_2Al$ has been reported within the range of 3.6 μ_B [6] to 4.12 μ_B [7]; therefore, it is not unreasonable for the model to suggest that the deformed + annealed sample has also experienced a fractional decrease in saturation magnetization. Ultimately, despite the fact that the model assumes the mean fault widths align with the fault widths of long, straight dislocations, it remains clear that the antiferromagnetically coupled faults bounded by partial dislocations studied here are a primary mechanism of the reduction in saturation magnetization within Mn-based $L2_1$-ordered intermetallics. An exciting avenue for future work would surely be to investigate the sensitivity of the fractional decrease in saturation magnetization to more elaborate arrangements of faulted material.

V. CONCLUSIONS

In conclusion, we report on a giant magnetoplastic effect in the $L2_1$-ordered intermetallic $MnCu_2Al$, brought about through plastic deformation that introduces crystalline defects with stacking disregistries that promote antiferromagnetic coupling. These large changes in macroscopic magnetic response are reversible by heat treatments that drive recrystallization and mitigation of the magnetically distinct defect populations. These results provide new insight into the class of spatially extended defect structures that host local magnetic states that differ from those expected of the bulk material, and can be used to manipulate the macroscopic properties of

the material simply by controlling the density of dissociated dislocations present. Exploring additional measures of control of magnetic properties through elastic strain effects surrounding undissociated dislocation cores and segregation of magnetic solute to dislocation cores provides additional mesoscale avenues to either increase or decrease macroscopic magnetization, and/or induce exotic strain textures. Defects may be further exploited to modify magnetization processes within a material system where the magnetic exchange interactions are acutely sensitive to atomic displacements. However, the study of these processes will require both the careful extension of micromagnetics theory and additional atomistic calculations. Our work also implies that various methods of magnetic characterization are attractive nondestructive approaches for characterizing the degree of deformation, chemical order, or degradation within any given material system, either at a macroscopic or individual defect level. Collectively, our work points to avenues for strong magnetoplastic control in other chemically complex systems (e.g., high entropy alloys) where competing spin interactions and a multiplicity of defect structures may exist, as well as pathways for either retarding or inducing plastic deformation via external magnetic fields.

ACKNOWLEDGMENTS

We gratefully thank Marc De Graef and Derick Ober for useful discussions and Christian Kübel and Xiaoke Mu for conducting initial experiments that guided our study. We acknowledge support by the Department of Energy, National Nuclear Security Administration under Award No. DE-NA0004152. We also thank CNRS for funding within the joint collaboration between IM2NP and UCSB via the IRP CNRS DASEIN project and the ESRF for allocating beam time (Experiment No. A32-2-844). We thank J-S. Micha, R. R. P. Purushottam, and O. Robach for assistance during the experiment at beamline BM32. The research reported here made use of the UC Santa Barbara NSF Quantum Foundry facilities funded via the Q-AMASE-i program under Award No. DMR-1906325, as well as the shared facilities of the Materials Research Science and Engineering Center (MRSEC) at UC Santa Barbara: NSF DMR–2308708. Use was made of the computational facilities administered by the Center for Scientific Computing at the CNSI and MRL (an NSF MRSEC; DMR–2308708) and purchased through NSF CNS-1725797. Use of the Advanced Photon Source at Argonne National Laboratory was supported by the U.S. Department of Energy, Office of Science, Office of Basic Energy Sciences, under Contract No. DE-AC02-06CH11357. J.A.M gratefully acknowledges support from the US NSF Graduate Research Fellowship Program under Grant No. NSF DGE-2139319. W.S.C. acknowledges support from the U.S. National Science Foundation MPS-Ascend Postdoctoral Research Fellowship under Grant No. 2316692. Any opinions, findings, and conclusions or recommendations expressed in this material are those of the author(s) and do not necessarily reflect the views of the National Science Foundation. B.E.R. gratefully acknowledges support from the U.S. Department of Defense (DoD) through the National Defense Science & Engineering Graduate (NDSEG) Fellowship Program.

DATA AVAILABILITY

The data that support the findings of this article are not publicly available upon publication because it is not technically feasible and/or the cost of preparing, depositing, and hosting the data would be prohibitive within the terms of this research project. The data are available from the authors upon reasonable request.

APPENDIX A: WILLIAMSON-HALL ANALYSES

1. Deconvolution of the instrument resolution function

To determine the extent of sample-induced peak broadening in the $L2_1$-ordered intermetallic powders, an instrument resolution function (IRF) was parametrized using the NIST Si 640d calibration standard, with a particle size of 600 μm. Peak full width at half maximum (FWHM) of calibration standard peaks were measured using the TCHZ peak type [32], which represents an analytic approximation to the convolution of Gaussian and Lorentzian components used to fit the experimental data. The IRF then deconvoluted from the measured spectra by decomposing the FWHM to the Gaussian and Lorentzian components, via

$$fwhm_G = \sqrt{U\tan^2\theta + V\tan\theta + \frac{Z}{\cos^2\theta}} \tag{A1}$$

and

$$fwhm_L = Z\tan\theta + \frac{Y}{\cos\theta}, \tag{A2}$$

where θ is the peak position, converted to peak breadths (β) via

$$\beta_G = \frac{1}{2} fwhm_G \left(\frac{\pi}{\ln 2}\right)^{\frac{1}{2}} \tag{A3}$$

and

$$\beta_L = \frac{\pi\, fwhm_L}{2}, \tag{A4}$$

then used to deconvolute the effects of instrument induced broadening from the measured breadths via

$$\beta_{G,\text{sample}} = \sqrt{\beta^2_{G,\text{measured}} - \beta^2_{G,\text{instrument}}} \tag{A5}$$

and

$$\beta_{L,\text{sample}} = \beta_{L,\text{measured}} - \beta_{L,\text{instrument}}. \tag{A6}$$

The sample-induced broadening β_{sample} was taken by recombining the Gaussian and Lorentzian components via

$$\beta_{\text{sample}} = \beta_{G,\text{sample}} + \beta_{L,\text{sample}}. \tag{A7}$$

In all cases, the IRF contribution to the measured β was found to be $<1\%$ of the measured β [33].

2. Conventional Williamson-Hall analysis

Conventional Williamson-Hall analysis is a metric of two factors in the line broadening of x-ray diffraction peaks: crystallite size and lattice strain [35]. By measuring the peak breadth β_{hkl}, and angle θ_{hkl} of a diffraction peak, the Williamson-Hall construct can be employed to determine

the average lattice strains ϵ and volume-weighted coherent diffracting domain (D_{Vol}) via

$$\beta\cos\theta = \frac{k\lambda}{D_{\text{Vol}}} + 2\epsilon\sin\theta. \tag{A8}$$

The impact of crystallite size on the peak breadth is independent of $2\epsilon\sin\theta$, and thus is extracted from the intercept (Y_0) of the Williamson-Hall plot. Here, λ is the wavelength of the x-rays in Ångströms, and k is a shape-anisotropy term which is generally taken as 1.0 in the case of isotropic particles [42]. Conversely, ϵ is dependent on $2\epsilon\sin\theta$, and may be extracted from the slope of the plot.

3. Direct-fit Williamson-Hall analysis

Microstrain anisotropy induced by the highly anisotropic elastic modulus of $MnCu_2Al$, is evident in the pristine and deformed powders. Following the approach by Takaki *et al.* [37] and Takaki *et al.* [38], the effect of elastic anisotropy is corrected via

$$\beta_{hkl}\cos\theta_{hkl} = \frac{k\lambda}{D_{hkl}} + \frac{\epsilon^*\sin\theta_{hkl}}{\omega_{hkl}}, \tag{A9}$$

enabling more accurate determination for crystallite sizes and strains. Here, ϵ^* is the true microstrain experienced by the crystal,

$$\omega_{hkl} = \frac{E^*_{hkl}}{E_0}, \tag{A10}$$

wherein E^*_{hkl} is the diffraction Young's modulus, and E_0 is the isotropic diffraction Young's Modulus. Diffraction Young's modulus is the stiffness measured by diffraction in a given {hkl} direction and its ratio to E_0 quantifies the extent to which the stiffness is anisotropic, i.e., sensitive to the relation between applied stress and the lattice strain in a given crystallographic direction. This orientation-dependent contribution to strain broadening may be omitted for materials that are nearly elastically isotropic materials, but is necessary for elastically anisotropic materials. This concept is nicely illustrated by the difference between Fig. 3(d) (no elastic correction) and Fig. 3(e) (with elastic correction) [37]. We apply the Kröner method [40,41] to relate the stiffness constants C_{ij} measured by Michelutti *et al.* [39] to the diffraction Young's modulus (E^*_{hkl}). The resulting direct-fit Williamson-Hall analysis, which minimizes the effect of anisotropic elasticity, enables accurate fitting of ϵ^* and D_{Vol}, which we next use to determine defect density via a modified Williamson-Hall fit. Although crystallite size estimates through Williamson-Hall analysis are not considered quantitative when the estimate is greater than 100 nm, there are slight qualitative differences in the estimates obtained from these powder samples.

4. Quantification of defect density via modified Williamson-Hall fits

Utilizing the conventional Williamson-Hall and direct-fit Williamson-Hall fits to extract D_{Vol} [37,38], we are able to extract the screw to edge ratio (S) in addition to the defect density (ρ) using the modified Williamson-Hall [36], rather than relying on prior characterization or estimation of S. For convenience, we define a parameter

$$\alpha = \frac{k}{D_{\text{Vol}}}, \tag{A11}$$

at this time. Following the approach by Ungár and Borbély, we next plot our data in the form of

$$(\Delta K - \alpha)^2/K^2 = \phi^2 C_{h00}(1 - qA_{hkl}), \tag{A12}$$

wherein we have defined

$$\Delta K = \frac{\beta\cos\theta}{\lambda} \tag{A13}$$

and

$$K = \frac{2\sin\theta}{\lambda}. \tag{A14}$$

$$K = \frac{2\sin\theta}{\lambda}.A_{hkl} = (h^2k^2 + k^2l^2 + l^2h^2)/(h^2 + k^2 + l^2) \tag{A15}$$

defines the direction cosines given by the diffracting plane indices hkl and α is defined by Eq. (A11). ϕ and q are determined by plotting in the form of $(\Delta K - \alpha)^2/K^2$ vs A_{hkl}, wherein ϕ is related to the intercept and q is related to the slope.

The screw component of the dislocations (S) is determined via

$$q = (1 - S)q^E + Sq^S, \tag{A16}$$

wherein q^E and q^S are estimated from the values tabulated by Úngar *et al.* [42], using inputs of the stiffness constants C_{ij} measured by Michelutti *et al.* [39], and under the assumption of $\langle 111\rangle\{110\}$ slip activity [26,28].

Dislocation density (ρ) is calculated from ϕ, by setting

$$\phi = \left(\frac{Y_0}{C_{h00}}\right)^{\frac{1}{2}}, \tag{A17}$$

equal to

$$\phi = \left(\frac{\pi}{2}\right)^{1/2} R_e b\rho. \tag{A18}$$

Here, Y_0 is the y intercept of

$$(\Delta K - \alpha)^2/K^2 = \phi^2 C_{h00}(1 - qA_{hkl}). \tag{A19}$$

The contrast factors C_{h00} are given by

$$C_{h00} = (1 - S)C^E_{h00} + SC^S_{h00}, \tag{A20}$$

where C^E_{h00} and C^S_{h00} are the contrast factors for edge and screw dislocations [42], given as a function of Zener anisotropy and C_{12}/C_{44}, calculated from the stiffness constants C_{ij} measured by Michelutti *et al.* [39]. R_e is the dislocation cutoff radius given as $R_e = 2b$, b is the full Burgers vector magnitude for $MnCu_2Al$, $b = a\sqrt{3}$ [28,64,87], where a is the cubic lattice parameter of $MnCu_2Al$, given by the experimental Rietveld refinements as $a = 5.95$ Å.

We note that the fitting parameters used to fit our data were developed for BCC alloys with relatively isotropic elastic properties, $\langle 111\rangle\{110\}$ slip, and undissociated dislocations. These fitting parameters are an oversimplification even for BCC alloys that exhibit $\langle 111\rangle\{112\}$, $\langle 111\rangle\{123\}$, or

TABLE I. Defect contents calculated for $MnCu_2Al$ in the deformed + annealed and deformed states using the direct-fit, conventional, and modified Williamson-Hall methods [35–37], including coherently diffracting domain size D_{Vol}, isotropic microstrain ϵ^*, microstrains resolved onto the {111} and {100} planes $\epsilon_{\{111\}}$ and $\epsilon_{\{100\}}$, the screw ratio of defects S, and dislocation density ρ.

	deformed + annealed	deformed
	conventional Williamson-Hall	
$\epsilon_{\{111\}}$	0.46%	1.43%
$\epsilon_{\{100\}}$	0.78%	3.27%
	direct-fit Williamson-Hall	
ϵ^*	0.69%	2.4%
D_{Vol}	185 nm	139 nm
	modified Williamson-Hall	
S	47%	86%
ρ	7.7×10^{15} m^{-2}	2.6×10^{16} m^{-2}

⟨111⟩{134} slip modes in addition to ⟨111⟩{110} slip. They also fail to account for twinning/antitwinning asymmetries in ⟨111⟩{112} slip modes. They are even less well suited to BCC-derived intermetallics, which exhibit anisotropic elastic properties, the slip mode complications described in the previous lines, and dissociated dislocations. However, to our knowledge, more appropriate fitting parameters do not yet exist to treat scattering data for BCC-derived intermetallics. In our fits, we have advanced the fits for BCC alloys to compensate for the large elastic anisotropy (more typically seen in FCC materials) using the models developed by Takaki *et al.* [37]. We hope that this topic is revisited once improved models have been developed for this material platform. At the present, we expect that our fits are not be quantitatively correct, but will be qualitatively correct when compared between datasets (see Table I).

APPENDIX B: DERIVING AN EXPRESSION FOR THE DECREASE IN SATURATION MAGNETIZATION AS A FUNCTION OF DISLOCATION DENSITY

1. An expression for the fractional decrease in saturation magnetization

Equation (6) is derived based primarily on the work of Ikeda and Takahashi [19], which we review here for completeness. Following their work, we begin by expressing the saturation magnetization of a Mn-based $L2_1$-ordered intermetallic as

$$M_s = [N_0 - N_{\rm I} - N_{\rm II}]\mu^0_{\rm Mn} + N_{\rm I}\mu^{\rm I}_{\rm Mn} + N_{\rm II}\mu^{\rm II}_{\rm Mn}, \tag{B1}$$

where 0, I, and II are used to represent the number of atoms located at the Mn site, the fault I site, and the fault II site, depicted within Fig. 7(d). Rearranging, we may express a change in M_s, relative to $N_0\mu^0_{\rm Mn}$ as

$$\left[M_s - N_0\mu^0_{\rm Mn}\right] = \Delta M_s = N_{\rm I}\left[\mu^{\rm I}_{\rm Mn} - \mu^0_{\rm Mn}\right] + N_{\rm II}\left[\mu^{\rm II}_{\rm Mn} - \mu^0_{\rm Mn}\right]. \tag{B2}$$

Dividing through by $N_0\mu^0_{\rm Mn}$, the fractional decrease in saturation magnetization, $\Delta M_s/M^0_s$, is then

$$\frac{\Delta M_s}{N_0\mu^0_{\rm Mn}} = \Delta M_s/M^0_s = f_{\rm I}\left[\frac{\mu^{\rm I}_{\rm Mn}}{\mu^0_{\rm Mn}} - 1\right] + f_{\rm II}\left[\frac{\mu^{\rm II}_{\rm Mn}}{\mu^0_{\rm Mn}} - 1\right] = f_{\rm I}[\alpha^{\rm I} - 1] + f_{\rm II}[\alpha^{\rm II} - 1]. \tag{B3}$$

Therefore, the fractional decrease in saturation magnetization is a function of both the fraction of Mn atoms located at irregular Mn sites corresponding to fault I ($f_{\rm I} = N_{\rm I}/N_0$), or fault II ($f_{\rm II} = N_{\rm II}/N_0$), and the ratio between the magnetic moment of Mn located on sites associated with either fault I, $\mu^{\rm I}_{\rm Mn}/\mu^0_{\rm Mn}$, or fault II, $\mu^{\rm II}_{\rm Mn}/\mu^0_{\rm Mn}$. To proceed, it is convenient to assume that $\mu^{\rm I}_{\rm Mn} = \mu^{\rm II}_{\rm Mn} = -\mu^0_{\rm Mn}$, meaning $\alpha^{\rm I} = \alpha^{\rm II} = -1$. $\Delta M_s/M^0_s$ is therefore dependent on how the exact dislocation configuration influences $f_{\rm I}$ and $f_{\rm II}$. As outlined in Fig. 6(e), we assume $f_{\rm I}$ and $f_{\rm II}$ are primarily influenced by the number of adjacent slip planes participating in the formation of the faulted, antiferromagnetic ribbon, and the dislocation density. Specifically

$$\frac{\Delta M_s}{M^0_s}(d_{\rm slip}, \rho) = -2[f_{\rm I}(d_{\rm slip}, \rho) + f_{\rm II}(d_{\rm slip}, \rho)]. \tag{B4}$$

2. Linking $f_{\rm I}$ and $f_{\rm II}$ to dislocation density

If the total line length of dislocation per unit volume—i.e., the total dislocation density ρ (units of [length/length^3])—is measurable, and one assumes that all dislocations dissociate based on Eq. (1). One may develop an expression for the fraction of irregular sites occupied by Mn, by considering the area of faulted crystal per unit volume of total crystal $\bar{A}_i$ (units of [length]/[length^2]), associated with fault I and fault II,

$$\bar{A}_{\rm I}(\rho) = 2\rho_{\rm I} w_{\rm I}(\rho) = \frac{\rho w_{\rm I}(\rho)}{2}, \tag{B5}$$

$$\bar{A}_{\rm II}(\rho) = \rho_{\rm II} w_{\rm II}(\rho) = \frac{\rho w_{\rm II}(\rho)}{4}. \tag{B6}$$

The fraction of irregular Mn atoms associated with fault I and fault II is then identical to the fractional volume $\bar{V}_i$ of material that has undergone a change in stacking associated with either of these faults. Assuming n adjacent slip planes take part in the formation of a faulted ribbon of material, $d_{\rm slip} = \frac{na_0}{\sqrt{2}}$,

$$\bar{V}_{\rm I}(d_{\rm slip}, \rho) = f_{\rm I}(n, a_0, \rho) = \frac{na_0}{2\sqrt{2}}[\rho w_{\rm I}(\rho)], \tag{B7}$$

$$\bar{V}_{\rm II}(d_{\rm slip}, \rho) = f_{\rm II}(n, a_0, \rho) = \frac{na_0}{4\sqrt{2}}[\rho w_{\rm II}(\rho)]. \tag{B8}$$

Within the following subsection we highlight three distinct scenarios under which $f_{\rm I}$ and $f_{\rm II}$ may be computed.

3. Analytical expressions for the fractional decrease in saturation magnetization

It is important to recall that by defining an area fraction and volume fraction of faulted material we are considering fault widths, $w_{\rm I}$ and $w_{\rm II}$, as representative fault widths that average over every element of faulted material. Without a more detailed model, we must hypothesize the form of these functions. There are three straightforward simplifications that are worth considering here.

a. The partials, on average, maintain a faulted region analogous to that observed for a long, straight full dislocation

Under this assumption, which is referred to as case (i) in the text, we approximate the average fault width of material as a weighted sum of the fault widths predicted using the phase-field approach of Rhodes *et al.* [28] In short, this approximation assumes that while the dislocation density is certainly high, the dislocation reactions expected for single, straight, dislocations within $MnCu_2Al$ may still serve as a reasonable proxy for the average fault widths. Specifically, w_{I} and w_{II} become

$$w_{\mathrm{I}} = (1-S)w_{\mathrm{I}}^{e} + Sw_{\mathrm{I}}^{s}, \tag{B9}$$

$$w_{\mathrm{II}} = (1-S)w_{\mathrm{II}}^{e} + Sw_{\mathrm{II}}^{s}, \tag{B10}$$

and these may be substituted in the expression for $[\Delta M_s]^{\mathrm{frac}}$,

$$[\Delta M_s]^{\mathrm{frac}}(n, a_0, \rho) = -\frac{na_0}{2\sqrt{2}}[2\rho w_{\mathrm{I}} + \rho w_{\mathrm{II}}]. \tag{B11}$$

b. Only the partials with the lowest fault energy distribute themselves homogeneously

There is certainly a situation wherein the dislocation density reaches a critical level such that the effective fault widths, w_{I} and w_{II}, deviate significantly from the zero applied stress configuration outlined above. As discussed by Ikeda and Takahashi [19], the dislocation density may reach a value where the faults begin to distribute themselves a mean area of $A_i = 1/\rho_i$, meaning the effective fault width will be of width $w_i = 1/\sqrt{\rho_i}$. Since the dissociation reaction of $\langle 111\rangle\{110\}$ dislocations within the family of $L2_1$ intermetallics involves two crystallographically distinct stacking faults with differing fault energies, this deviation may occur in stages. First, the fault with the lowest fault energy—fault II—may distribute itself over the material system's volume, leading to an expression for $\Delta M_s/M_s^0$ of the form

$$\frac{\Delta M_s}{M_s^0}\left(n, a_0, \rho > \rho_{\mathrm{II}}^{c}\right) = -\frac{na_0}{2\sqrt{2}}[2\rho w_{\mathrm{I}}(\rho) + \sqrt{\rho}]. \tag{B12}$$

This is case (ii) within Fig. 6(e).

c. All partials distribute themselves homogeneously

Alternatively, the dislocation density may reach a density that is large enough to promote the redistribution of all partials, leading to the following expression for $\Delta M_s/M_s^0$,

$$\frac{\Delta M_s}{M_s^0}\left(n, a_0, \rho > \rho_{\mathrm{I}}^{c} > \rho_{\mathrm{II}}^{c}\right) = -\frac{3na_0}{2\sqrt{2}}\sqrt{\rho}. \tag{B13}$$

This is referred to as case (iii) in Fig. 6(e).

[1] O. Gutfleisch, M. A. Willard, E. Brück, C. H. Chen, S. Sankar, and J. P. Liu, Magnetic materials and devices for the 21st century: Stronger, lighter, and more energy efficient, Adv. Mater. **23**, 821 (2011).

[2] G. Bertotti, Connection between microstructure and magnetic properties of soft magnetic materials, J. Magn. Magn. Mater. **320**, 2436 (2008).

[3] M. Ali and F. Ahmad, A review of processing techniques for Fe-Ni soft magnetic materials, Mater. Manuf. Process. **34**, 1580 (2019).

[4] D. C. Jiles, Dynamics of domain magnetization and the Barkhausen effect, Czech. J. Phys. **50**, 893 (2000).

[5] L. Weissitsch, F. Staab, K. Durst, and A. Bachmaier, Magnetic materials via high-pressure torsion of powders, Mater. Trans. **64**, 1537 (2023).

[6] T. Shinohara, Contribution of $s-d$ interaction to the internal magnetic field in Heusler alloys, J. Phys. Soc. Jpn. **27**, 1127 (1969).

[7] D. Oxley, R. Tebble, and K. Williams, Heusler alloys, J. Appl. Phys. **34**, 1362 (1963).

[8] F. Heusler, W. Starck, and E. Haupt, Magnetisch-chemische studien, Verh. Dtsch. Phys. Ges **5**, 219 (1903).

[9] T. Graf, C. Felser, and S. S. Parkin, Simple rules for the understanding of Heusler compounds, Prog. Solid State Chem. **39**, 1 (2011).

[10] J. Kübler, A. R. William, and C. B. Sommers, Formation and coupling of magnetic moments in heusler alloys, Phys. Rev. B **28**, 1745 (1983).

[11] G. Malmstrom, D. Geldart, and C. Blomberg, Interaction between local magnetic moments in metals. I, J. Phys. F **6**, 233 (1976).

[12] E. Şaşıoğlu, L. M. Sandratskii, and P. Bruno, Role of conduction electrons in mediating exchange interactions in Mn-based Heusler alloys, Phys. Rev. B **77**, 064417 (2008).

[13] E. Şaşıoğlu, L. M. Sandratskii, P. Bruno, and I. Galanakis, Exchange interactions and temperature dependence of magnetization in half-metallic Heusler alloys, Phys. Rev. B **72**, 184415 (2005).

[14] Y. Kurtulus, M. Gilleßen, and R. Dronskowski, Electronic structure, chemical bonding, and finite-temperature magnetic properties of full Heusler alloys, J. Comput. Chem. **27**, 90 (2006).

[15] Y. Noda and Y. Ishikawa, Spin waves in Heusler alloys Pd_2MnSn and Ni_2MnSn, J. Phys. Soc. Jpn. **40**, 690 (1976).

[16] K. Tajima, Y. Ishikawa, P. J. Webster, M. W. Stringfellow, D. Tocchetti, and K. R. Zeabeck, Spin waves in a Heusler alloy Cu_2MnAl, J. Phys. Soc. Jpn. **43**, 483 (1977).

[17] A. Lapworth and J. Jakubovics, Effect of antiphase boundaries on the magnetic properties of Cu-Mn-Al Heusler alloys, Philos. Mag. **29**, 253 (1974).

[18] M. Bouchard, Electron metallography and magnetic properties Cu-Mn-Al Heusler alloys, Ph.D. thesis, Imperial College, 1970.

[19] K. Ikeda and S. Takahashi, Cold-working effect on magnetic properties in the Heusler alloys, Phys. Rev. B **30**, 3808 (1984).

[20] T. Kamiyama, T. Shinohara, S. Tomiyoshi, Y. Minonishi, H. Yamamoto, H. Asano, and N. Watanabe, Effect of deformation on Pd_2MnSn Heusler alloy studied with transmission electron microscopy, profile analysis of neutron powder diffraction pattern, and magnetization measurement, J. Appl. Phys. **68**, 4741 (1990).

[21] S. Takahashi and T. Shinohara, Magnetic moment distribution in deformed Heusler alloy Pd_2MnSn, J. Phys. F **12**, 3115 (1982).

[22] E. E. Levin, D. A. Kitchaev, Y. M. Eggeler, J. A. Mayer, P. Behera, D. S. Gianola, A. Van der Ven, T. M. Pollock, and R. Seshadri, Influence of plastic deformation on the magnetic properties of Heusler $MnAu_2Al$, Phys. Rev. Mater. **5**, 014408 (2021).

[23] S. Venkateswaran, N. Nuhfer, and M. De Graef, Anti-phase boundaries and magnetic domain structures in Ni_2MnGa-type Heusler alloys, Acta Mater. **55**, 2621 (2007).

[24] L. Straka, L. Fekete, and O. Heczko, Antiphase boundaries in bulk Ni-Mn-Ga Heusler alloy observed by magnetic force microscopy, Appl. Phys. Lett. **113**, 172901 (2018).

[25] L. Straka, L. Fekete, M. Rameš, E. Belas, and O. Heczko, Magnetic coercivity control by heat treatment in Heusler Ni–Mn–Ga (–B) single crystals, Acta Mater. **169**, 109 (2019).

[26] M. L. Green, G. Chin, and J. Vander Sande, Plastic deformation of single crystals of the Heusler alloy Cu_2MnAl, Metall. Trans. A **8**, 353 (1977).

[27] M. Yamaguchi and Y. Umakoshi, The deformation behaviour of intermetallic superlattice compounds, Prog. Mater. Sci. **34**, 1 (1990).

[28] B. E. Rhodes, J. A. Mayer, S. Xu, J. D. Lamb, J. Wendorf, M. P. Echlin, T. M. Pollock, Y. M. Eggeler, I. J. Beyerlein, and D. S. Gianola, Deformation mechanisms and defect structures in Heusler intermetallic $MnCu_2Al$, Acta Mater. **268**, 119711 (2024).

[29] B. Dubois and D. Chevereau, Decomposition of the Heusler alloy Cu_2MnAl at 360°C, J. Mater. Sci. **14**, 2296 (1979).

[30] B. E. Rhodes, P. Garg, N. M. della Ventura, J. A. Mayer, I. J. Beyerlein, and D. S. Gianola, Deformation pseudo-twinning of the l21-ordered intermetallic superlattice, Scr. Mater. **257**, 116468 (2025).

[31] B. E. Rhodes, S. Comby-Dassonneville, T. W. Cornelius, O. Thomas, I. J. Beyerlein, and D. S. Gianola, *In situ* laue microdiffraction tracking of the 110 to 112 slip mode transition in $L2_1$-ordered $MnCu_2AL$, J. Mater. Res. Technol. **41**, 6748 (2026).

[32] P. Thompson, D. Cox, and J. Hastings, Rietveld refinement of Debye–Scherrer synchrotron x-ray data from Al_2O_3, J. Appl. Cryst. **20**, 79 (1987).

[33] A. A. Coelho, *TOPAS* and *TOPAS-Academic*: An optimization program integrating computer algebra and crystallographic objects written in C + +, J. Appl. Cryst. **51**, 210 (2018).

[34] K. Momma and F. Izumi, *VESTA 3* for three-dimensional visualization of crystal, volumetric and morphology data, J. Appl. Cryst. **44**, 1272 (2011).

[35] G. Williamson and W. Hall, X-ray line broadening from filed aluminium and wolfram, Acta Metall. **1**, 22 (1953).

[36] T. Ungár and A. Borbély, The effect of dislocation contrast on x-ray line broadening: A new approach to line profile analysis, Appl. Phys. Lett. **69**, 3173 (1996).

[37] S. Takaki, F. Jiang, T. Masumura, and T. Tsuchiyama, Correction of elastic anisotropy in Williamson-Hall plots by diffraction Young's modulus and direct fitting method, ISIJ Intl. **58**, 769 (2018).

[38] S. Takaki, T. Masumura, and T. Tsuchiyama, Dislocation characterization by the direct-fitting/modified Williamson–Hall (DF/mWH) method in cold worked ferritic steel, ISIJ Intl. **59**, 567 (2019).

[39] B. Michelutti, R. P. de La Bathie, E. d. T. de Lacheisserie, and A. Waintal, Magnetization, magnetocrystalline anisotropy, magnetostriction and elastic constants of the Heusler alloy: Cu_2MnAl, Solid State Commun. **25**, 163 (1978).

[40] E. Kröner, Berechnung der elastischen konstanten des vielkristalls aus den konstanten des einkristalls, Z. Phys. **151**, 504 (1958).

[41] Z. Wang, A. D. Stoica, D. Ma, and A. M. Beese, Diffraction and single-crystal elastic constants of Inconel 625 at room and elevated temperatures determined by neutron diffraction, Mater. Sci. Eng. A **674**, 406 (2016).

[42] T. Ungár, I. Dragomir, Á. Révész, and A. Borbély, The contrast factors of dislocations in cubic crystals: The dislocation model of strain anisotropy in practice, J. Appl. Cryst. **32**, 992 (1999).

[43] M. Wilkens, The determination of density and distribution of dislocations in deformed single crystals from broadened x-ray diffraction profiles, Phys. Stat. Sol. (a) **2**, 359 (1970).

[44] J. A. Simmons, R. De Wit, and R. Bullough, *Fundamental Aspects of Dislocation Theory: Conference Proceedings, National Bureau of Standards 1969* (US National Bureau of Standards, 1970), Vol. 1.

[45] https://www.fabiocrameri.ch/colourmaps/.

[46] D. N. Johnstone, B. H. Martineau, P. Crout, P. A. Midgley, and A. S. Eggeman, Density-based clustering of crystal (mis) orientations and the *orix* python library, J. Appl. Cryst. **53**, 1293 (2020).

[47] J. Micha, Lauetools: Open source python packages for x-ray microlaue diffraction analysis (2014), https://gitlab.esrf.fr/micha/lauetools.

[48] R. Purushottam Raj Purohit, S. Tardif, O. Castelnau, J. Eymery, R. Guinebretière, O. Robach, J. Micha, *et al.*, LaueNN: Neural network based hkl recognition of Laue spots and its application to polycrystalline materials, Acta Cryst. A **78**, a225 (2022).

[49] B. H. Savitzky, S. E. Zeltmann, L. A. Hughes, H. G. Brown, S. Zhao, P. M. Pelz, T. C. Pekin, E. S. Barnard, J. Donohue, L. R. DaCosta, *et al.*, py4DSTEM: A software package for four-dimensional scanning transmission electron microscopy data analysis, Microsc. Microanal. **27**, 712 (2021).

[50] See Supplemental Material at http://link.aps.org/supplemental/10.1103/k8bj-j1tp for additional figures, tables, and text.

[51] G. Kresse and J. Furthmüller, Efficient iterative schemes for *ab-initio* total-energy calculations using a plane-wave basis set, Phys. Rev. B **54**, 11169 (1996).

[52] P. E. Blöchl, Projector augmented-wave method, Phys. Rev. B **50**, 17953 (1994).

[53] G. Kresse and D. Joubert, From ultrasoft pseudopotentials to the projector augmented-wave method, Phys. Rev. B **59**, 1758 (1999).

[54] J. P. Perdew, K. Burke, and M. Ernzerhof, Generalized gradient approximation made simple, Phys. Rev. Lett. **77**, 3865 (1996).

[55] H. J. Monkhorst and J. D. Pack, Special points for Brillouin-zone integrations, Phys. Rev. B **13**, 5188 (1976).

[56] J. G. Goiri and A. Van der Ven, MULTISHIFTER: Software to generate structural models of extended two-dimensional defects in 3D and 2D crystals, Comput. Mater. Sci. **191**, 110310 (2021).

[57] W. F. Brown Jr., Theory of the approach to magnetic saturation, Phys. Rev. **58**, 736 (1940).

[58] W. F. Brown Jr., The effect of dislocations on magnetization near saturation, Phys. Rev. **60**, 139 (1941).
[59] R. Herz and H. Kronmueller, High-field susceptibility of EuS single crystals, J. Magn. Magn. Mater. **15–18**, 1299 (1980).
[60] Z.-Q. Jin, W. Tang, J.-R. Zhang, H.-X. Qin, and Y.-W. Du, Effective magnetic anisotropy of nanocrystalline Nd-Fe-Ti-N hard magnetic alloys, Eur. Phys. J. B **3**, 41 (1998).
[61] H. Kronmüller, Micromagnetism and microstructure of amorphous alloys, J. Appl. Phys. **52**, 1859 (1981).
[62] R. M. Bozorth, *Ferromagnetism* (Wiley, New York, 1993).
[63] P. Shi, Magneto-elastoplastic coupling model of ferromagnetic material with plastic deformation under applied stress and magnetic fields, J. Magn. Magn. Mater. **512**, 166980 (2020).
[64] M. L. Green and G. Y. Chin, Deformation and fracture of polycrystalline Cu_2MnAl, Metall. Trans. **6**1118 (1975).
[65] A. Young and J. Jakubovics, The effect of planar defects on exchange interactions in ferromagnetic metals, J. Phys. F **5**, 1866 (1975).
[66] K. Edalati, A. Bachmaier, V. A. Beloshenko, Y. Beygelzimer, V. D. Blank, W. J. Botta, K. Bryła, J. Čížek, S. Divinski, N. A. Enikeev, *et al.*, Nanomaterials by severe plastic deformation: Review of historical developments and recent advances, Mater. Res. Lett. **10**, 163 (2022).
[67] H. Azzeddine, D. Bradai, T. Baudin, and T. G. Langdon, Texture evolution in high-pressure torsion processing, Prog. Mater. Sci. **125**, 100886 (2022).
[68] R. Z. Valiev, B. Straumal, and T. G. Langdon, Using severe plastic deformation to produce nanostructured materials with superior properties, Annu. Rev. Mater. Res. **52**, 357 (2022).
[69] Y. Zhao, H. Sheng, and K. Lu, Microstructure evolution and thermal properties in nanocrystalline Fe during mechanical attrition, Acta Mater. **49**, 365 (2001).
[70] H. Mughrabi, Dislocation wall and cell structures and long-range internal stresses in deformed metal crystals, Acta Metall. **31**, 1367 (1983).
[71] T. Ungar, H. Mughrabi, D. Rönnpagel, and M. Wilkens, X-ray line-broadening study of the dislocation cell structure in deformed [001]-orientated copper single crystals, Acta Metall. **32**, 333 (1984).
[72] C. Ophus, Four-dimensional scanning transmission electron microscopy (4D-STEM): From scanning nanodiffraction to ptychography and beyond, Microsc. Microanal. **25**, 563 (2019).
[73] J. W. Christian and S. Mahajan, Deformation twinning, Prog. Mater. Sci. **39**, 1 (1995).
[74] J. Christian, Some surprising features of the plastic deformation of body-centered cubic metals and alloys, Metall. Trans. A **14**, 1237 (1983).
[75] J. Christian and D. Laughlin, Twinning in derivative structures of BCC and FCC, Scr. Metall. **21**, 1131 (1987).
[76] E. Bertrand, P. Castany, I. Péron, and T. Gloriant, Twinning system selection in a metastable β-titanium alloy by Schmid factor analysis, Scr. Mater. **64**, 1110 (2011).
[77] J. A. Muñoz, R. E. Bolmaro, A. M. Jorge, A. Zhilyaev, and J. M. Cabrera, Prediction of generation of high-and low-angle grain boundaries (HAGB and LAGB) during severe plastic deformation, Metall. Mater. Trans. A **51**, 4674 (2020).
[78] O. Mishin, V. Y. Gertsman, R. Valiev, and G. Gottstein, Grain boundary distribution and texture in ultrafine-grained copper produced by severe plastic deformation, Scr. Mater. **35**, 873 (1996).
[79] J. Mackenzie, The distribution of rotation axes in a random aggregate of cubic crystals, Acta Metall. **12**, 223 (1964).
[80] V. Vitek, D. Smith, and R. Pond, Structure of tilt grain boundaries in bcc metals, Philos. Mag. A **41**, 649 (1980).
[81] D. Wolf, Correlation between the energy and structure of grain boundaries in bcc metals I. Symmetrical boundaries on the (110) and (100) planes, Philos. Mag. B **59**, 667 (1989).
[82] D. Wolf, Correlation between the energy and structure of grain boundaries in bcc metals. II. Symmetrical tilt boundaries, Philos. Mag. A **62**, 447 (1990).
[83] G. I. Taylor, Plastic strain in metals, J. Inst. Metals **62**, 307 (1938).
[84] R. Doherty, D. Hughes, F. Humphreys, J. J. Jonas, D. J. Jensen, M. Kassner, W. King, T. McNelley, H. McQueen, and A. Rollett, Current issues in recrystallization: A review, Mater. Sci. Eng. A **238**, 219 (1997).
[85] S. Gourdet and F. Montheillet, A model of continuous dynamic recrystallization, Acta Mater. **51**, 2685 (2003).
[86] L. Weissitsch, M. Stückler, S. Wurster, P. Knoll, H. Krenn, R. Pippan, and A. Bachmaier, Strain induced anisotropic magnetic behaviour and exchange coupling effect in Fe-$SmCo_5$ permanent magnets generated by high pressure torsion, Crystals **10**, 1026 (2020).
[87] Y. Umakoshi, M. Yamaguchi, and T. Yamane, Deformation and fracture behaviour of the Heusler alloy Cu_2MnAl single crystals, Acta Metall. **32**, 649 (1984).